NANOMECHANICAL BUCKLING FOR APPLICATIONS IN NONLINEAR DYNAMICS

A THESIS SUBMITTED TO

THE GRADUATE SCHOOL OF ENGINEERING AND SCIENCE

OF BILKENT UNIVERSITY

IN PARTIAL FULFILLMENT OF THE REQUIREMENTS FOR

THE DEGREE OF

MASTER OF SCIENCE

IN

MECHANICAL ENGINEERING

By

Berke Demiralp

July 2021

NANOMECHANICAL BUCKLING FOR APPLICATIONS IN NON-LINEAR DYNAMICS
By Berke Demiralp
July 2021

We certify that we have read this thesis and that in our opinion it is fully adequate, in scope and in quality, as a thesis for the degree of Master of Science.

Mehmet Selim Hanay(Advisor)

Emine Yegan Erdem

Alpan Bek

Approved for the Graduate School of Engineering and Science:

Ezhan Karaşan
Director of the Graduate School

ABSTRACT

NANOMECHANICAL BUCKLING FOR APPLICATIONS IN NONLINEAR DYNAMICS

Berke Demiralp
M.S. in Mechanical Engineering
Advisor: Mehmet Selim Hanay
July 2021

There has not been enough attention on post buckling behavior at nano scale even though it reveals rich nonlinear and chaotic dynamics and has potential to be used on cutting edge sensing, actuation, computation and communication applications. Here, full motion of the nanomechanical buckling, starting from unbuckled position to large deformations at post buckling regime has been precisely measured with error bars of ±7 nm for large deformation regime and ±2.8 nm for initial bending, with a noise floor of 38.5 pm/$\sqrt{Hz}$. Line mode of SEM is used for deflection detection which uses secondary electrons collected from sample and relevant code is developed for data processing. Initial bending, initial buckling and inflection point are well defined which can help us to understand transition to post buckling regime and development of sensors and actuators. Additionally, one well oscillation, double well oscillation and chaotic trajectories are investigated using the system as forced double well oscillator. Trajectory plotting is performed with an image processing code which benefits from contrast difference of the device and environment. A new region within double well oscillation regime is observed where motion converts from one well oscillation to double well oscillation which could be a candidate on mechanical computation and communication applications. Also, a preliminary design for synchronized chaos experiments using the same buckling platform is developed.

Finally, an optomechanical experimental setup and chip is built for measurement of one or multiple NEMS beams. Fiber optic techniques are used for experimental setup and grating couplers, ring/racetrack resonators are developed for beam measurements. Critical couplings on multiple devices are observed.

Keywords: NEMS, Buckling, Chaos, Chaotic Dynamics, Optomechanics.

ÖZET

DOĞRUSAL OLMAYAN DİNAMİK UYGULAMALARI İÇİN NANOMEKANİK BÜKÜLME

Berke Demiralp
Makine Mühendisliği, Yüksek Lisans
Tez Danışmanı: Mehmet Selim Hanay
Temmuz 2021

Nano boyuttaki bükülme sonrası davranışa, zengin, doğrusal olmayan ve kaotik dinamikleri ortaya çıkarmasına rağmen ve ileri teknoloji ölçüm, hareket, hesaplama ve iletişim teknolojilerinde kullanılma potensiyeli olmasına rağmen yeterli önem verilmemiştir. Burada, bükülme öncesi durumdan, bükülme sonrası alandaki büyük bükülmelere kadar olan nano mekanik kirişin tüm hareketi, büyük bükülmeler için ±7 nm ve başlangıç eğilmeleri için ±2.8 nm hata payı ve 38.5 pm/$\sqrt{Hz}$ gürültü taban seviyesi ile hassasiyetle ölçülmüştür. Bükülmeleri algılamak için numuneden ikincil elektronları toplayan taramalı elektron mikroskopunun çizgi modu kullanılmıştır ve data işleme adına uygun bir kod geliştirilmiştir. Bükülme sonrası geçişi anlamamıza ve sensor ve hareket ünitelerini oluşturmamıza yarayan başlangıç eğilmesi, başlangıç bükülmesi ve dönüm noktası düzgünce tanımlanmıştır. Bununla birlikte, sistemi, kuvvet barındıran iki kuyulu osilator olarak kullanarak, tek kuyu sallantısı, iki kuyu sallantısı ve kaotik yollar incelenmiştir. Yollar, cihaz ve çevresinin parlaklık farkından yararlanan bir görüntü işleme kodu ile elde edilmiştir. İki kuyu bölgesi arasında, tek kuyu sallantısından iki kuyu sallantısına geçiş yapan geçiş yapan ve mekanik hesaplama ve iletişim uygulamalarına aday olabilecek yeni bir bölge tespit edilmiştir. Aynı zamanda, aynı nano mekanik bükülme platformu kullanılarak senkronize kaos deneyleri için bir ön model geliştirilmiştir.

Son olarak, bir veya birkaç NEMS kirişinin ölçümü için optomekanik deney düzeneği ve yonga inşa edilmiştir. Deney düzeneği için fiber optik teknikleri kullanılmış, kiriş ölçümleri için ışık kırınım ızgaraları, halka/yarış pisti rezonatörleri geliştirilmiştir. Birkaç cihazda kritik ışık döngüsü gözlemlenmiştir.

Anahtar sözcükler: NEMS, Bükülme, Kaos, Kaotik Dinamikler, Optomekanik.

Acknowledgement

Starting with, I would like to thank Prof. Mehmet Selim Hanay for supervising me during my master studies. The work presented would not be possible without his help and support. Most importantly, I thank him for extending my knowledge and vision as a scientist and an engineer.

I thank to thank Prof. Emine Yegan Erdem for her teachings and support since my undergraduate years and I thank both Prof. Emine Yegan Erdem and Prof. Alpan Bek for joining my thesis defence, their time and valuable suggestions.

I would like to thank Prof. Michael Roukes for introducing the line mode idea to us.

I would like to thank Prof. Seymur Jahangirov for valuable and entertaining lessons on physics.

I thank Dr. Pisheh for teaching me nano manufacturing starting from the day I joined to Hanay Research Group and his friendship. I also would like to thank Berk Küçükoğlu for writing the Compact Rio codes for line mode experiments, designing the amplifier for chaos experiments and his friendship, Hakan Karakurt, Arda Seçme and Peyman Firoozy for the experiments we made and their friendship. Additionally, I thank all members of the Hanay Researach Group for their friendship and valuable discussions. I would like to thank Selçuk Oğuz Erbil, Utku Hatipoğlu for teaching me buckling project when I joined to group, Ezgi Orhan and Levent Aslanbaş for making the first introduction to the group and their friendship as well.

I thank Ahmet Murat Yağcı and Kadir Ulak for helping us with wirebonding processes and also all staff of UNAM for making fabrication process possible for us.

I thank ERC for supporting the buckling projects and TUBİTAK for supporting the optomechanics project.

I would like to thank Merve Çetiner, Atakan Atay, Didem Fatma Demir, Büşra Sarıarslan, Berkay Şahinoğlu, Alper Topuz, Emre Eraslan, Güray Baydur, Muhammed Baykal and all my other friends from Bilkent University for fun times.

I also thank my friends Mustafa Efe Çetin, Onur Zeki Güven, Fatih Çağatay Türkoğlu and Oğuzhan Kadir Başbuğ Güner for their friendship.

Most importantly, many thanks to my family who supported and helped me not only during my master studies, but through my entire lifetime with their unconditional love. The path I am following now, would not have been reachable to me without them.

Contents

List of Figures

List of Tables

Chapter 1

Introduction

Nanoelectromechanical systems (NEMS) are devices which are composed of coupled mechanical and electronical elements, having sub-micron dimensions. NEMS were initialized with studies done at 1996 and are commonly used as sensors, actuators and transducers in many fields due to their integrability to diverse applications [1–5]. NEMS also provide high quality factors [6, 7] and large scale integration possibility [8]. Reduction in the size of NEMS enabled researchers to detect single molecules [9] as well as individual protein macromolecules in real time [10]. With superposition of the modes, spatial distribution of a mass was demonstrated [11, 12]. Additionally, NEMS have been used on memory, switching and computational applications [13–17], some extending their operation to extreme environmental conditions where digital electronics fail [18, 19].

Although post buckling behavior opens avenues for applications such as transduction, computation [20] and investigation of rich nonlinear dynamics, a little attention has been paid to it in the past. Buckling at nano and micro scale has mostly accomplished with pre-stressed beams [21, 22] which restrains full control of the motion or by thermally, which results as significant heating and power consumption [23, 24] making those systems hard to integrate on large scale and use them in technological applications. In a recent study, researchers built a NEMS based nano buckling platform which enables precise tuning of the motion, starting from unbuckled position to large deformations at post buckling regime, without generation of the significant heat [25].

NEMS also enable optical integration and operation due to their size. Some applications include actuation [26], transduction [27] and sensing [28–31]. As a branch of sensing, ring/racetrack resonator combination is commonly used not just in nano beam sensing but also in chemical and biological sensing [32–36]. Combining nano dimensional structures with optics, researchers also achieved measurement imprecision levels that can enable detecting quantum phenomena in mechanical beams [37] and cooled down the mechanical beam into its ground state of motion [38]. Similar system has also potential to be used at optomechanical entanglement [39] and communication applications [40]. Manipulating waveguides mechanically was also a method for quantum communication applications [41]. Additionally, by deflecting mechanical structures, phase shifting of light was achieved [42].

In the present study, by using the same nanomechanical buckling platforms from the reference [25], motion of the beam is measured, starting from unbuckled position to large deformations at post buckling regime. Having a precise measurement with low error bars and low noise floor level at large deflections is critically important to further investigate the parameters of buckling to use those devices in technological applications such as actuators, transducers, and mechanical computers. Those parameters include but not limited to the initial bending, point where initiation of buckling starts, inflection point where second derivative of the trajectory is zero and spring softening occurs. An experimental procedure and data analyzation method is developed to ensure low error bars and noise floor level. Secondary electrons are collected from the device under SEM to measure deflection and a code is built to detect it. Error bars as low as ±7 nm for large deformation regime and ±2.8 nm for initial bending were detected with a noise floor of 38.5 pm/$\sqrt{Hz}$.

The aim of the first part of present study is to build the foundation and understand the system's static and dynamic behavior for the ERC project with the content of designing buckling actuators for bringing MW probes close to cellular surface for single and sub cellular sensing applications.

Additionally, chaotic dynamics, small and large oscillations of the beam are investigated at post buckling regime under SEM and trajectory is constructed by an image processing code. Since post buckling regime can be expressed as double well, voltage is applied to the buckled beam to show outcomes of forced double well oscillator. Strong evidence of chaotic trajectory, double and one well oscillations are observed. Also, an additional unexpected trajectory is observed which starts its oscillation at one well, then converts that motion to double well oscillation. Further, by decreasing the voltage it is found that probability of double well oscillation increased and time takes at one well oscillation is decreased.

Finally, series of ring and racetrack resonators are developed for single or multiple NEMS measurements. Grating couplers and waveguides are used to couple light from fiber to chip and to the ring resonator, respectively. A custom made low cost tilt stage is added to commercial XYZ stage which gives a larger tilt option than commercial devices. Several couplings are observed within resonators with some of them being critically coupled with a quality factor more than 1300 at room temperatures and pressures.

1.1 Thesis Outline

Chapter 1 gives a brief review of the recent studies at NEMS and their applications. Additionally, studies on combining light with NEMS structures is presented. Then, the work performed in this thesis is explained.

Chapter 2 explains the nanomechanical buckling architecture and its manufacturing process.

Chapter 3 starts with explaining the line mode measurement which can be performed under SEM. Then, deflection measurement experiment is detailly presented including the setup, experimental procedures, data analysis and results.

Chapter 4 includes forced double well experiments on nanomechanical buckling platform. In the beginning, bifurcation, double well analogy and their relevancy to the platform is explained. Then, experimental setup, procedures, data analysis and results are detailly presented.

Chapter 5 explains developing ring/racetrack resonators for NEMS and buckling deflection measurements. It starts with the waveguide - ring resonator model and derivation of coupling equations. Device architecture, fiber preparation and alignment procedures are also explained. Experiment setup, experimentation and results are presented at the end. Resonators built in this chapter could be used for sensing buckling deformation with higher sensitivity compared to the line mode measurements which were discussed at Chapter 3.

Chapter 6 includes conclusion and the future work.

Chapter 2

Architecture and Manufacturing of the Buckling Device

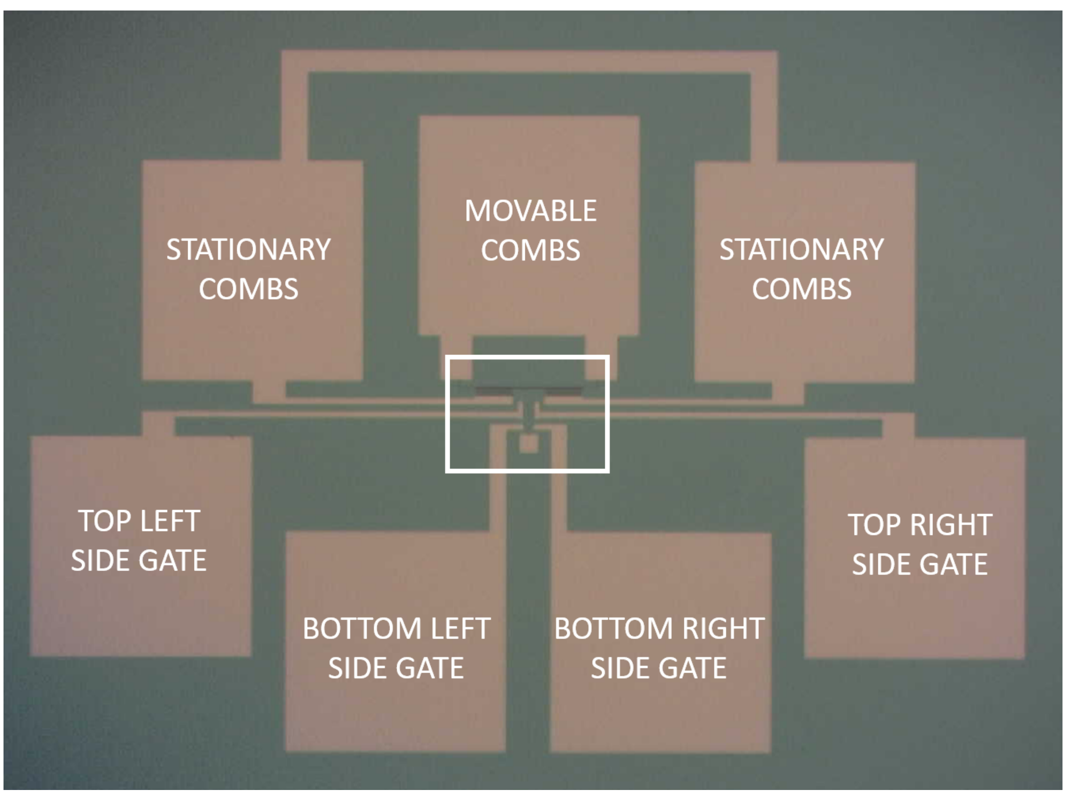

Figure 2.1: Device under optical microscope. Figure 2.2 is the section in the white rectangle.

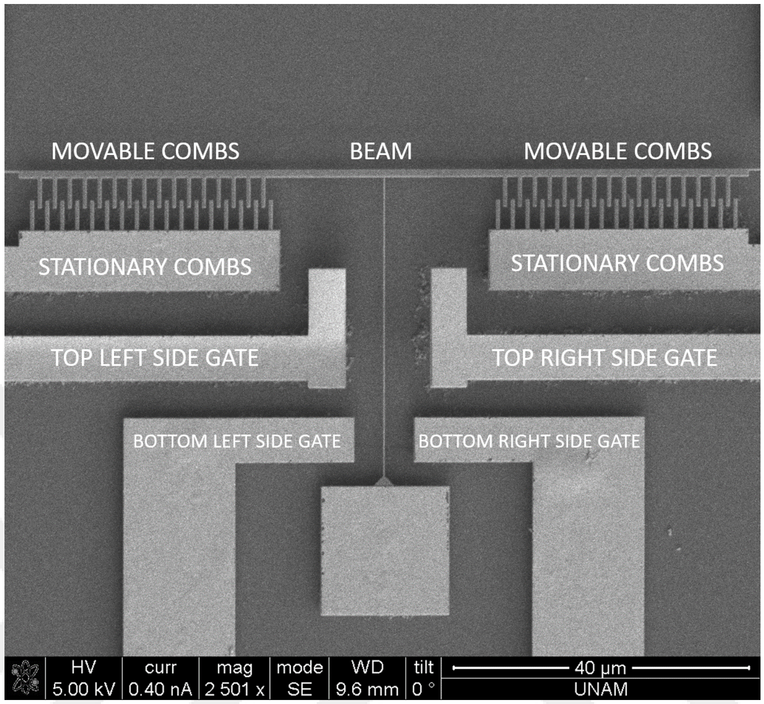

Figure 2.2: Buckling device under SEM.

The device is composed of two comb drive actuators, four side gates, a doubly clamped beam, electrical guides and contact pads. Voltage connections to contact pads are made by wire bonds from golden pads (Figure 2.1) to custom built PCB (Figure 2.3).

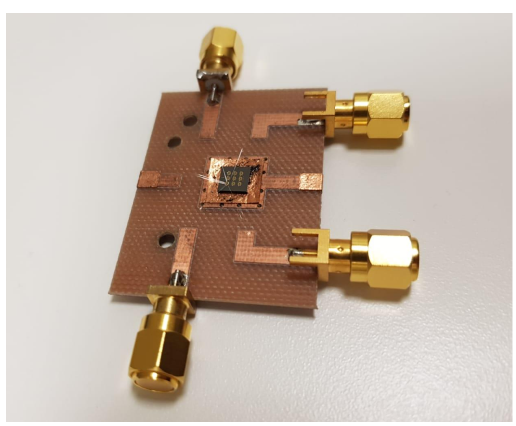

Figure 2.3: PCB with wire bonded device on it.

As voltage difference is applied to comb drive actuators a compression force is exerted on the beam. If the applied force exceeds the critical buckling force, the beam buckles either to the left or to the right. Critical buckling force is calculated as 290 nN, by taking Young's Modulus as 167.5 GPa and beam width, thickness and length as 150 nm, 250 nm and 40 µm, respectively. Parameters of the comb drive actuators are listed at Table 2.1. For calculation of the parameters, check the reference [43].

Length	4 µm
Width	500 nm
Thickness	250 nm
Distance between fingers	500 nm
Number of fingers (movable comb)	16
Number of fingers (stationary combs)	17

Table 2.1: Parameters for comb drive actuators.

Side gates are used for determining the direction of the buckling by applying a voltage to them. During the experiments that are included at this thesis, only the top pair of side gates are used. Bottom pair is at the ground level. Additionally, movable combs hence the beam is at ground level. For actuation, voltage is applied only to the stationary combs.

Detailed recipes for manufacturing the device can be found at the reference [43]. However, an additional manufacturing step was introduced for the sake of the work explained in this thesis, so it is beneficial to explain manufacturing steps from the beginning.

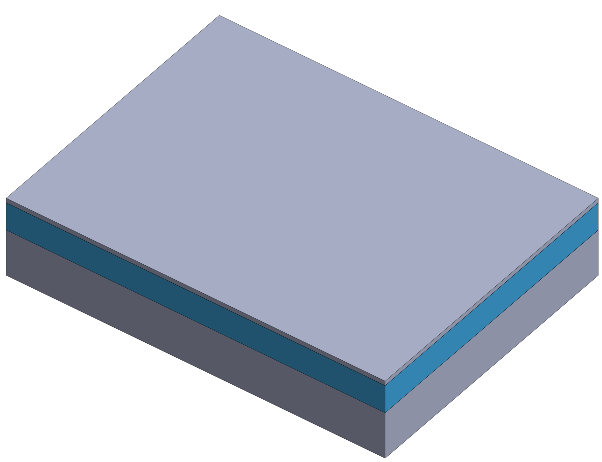

Wafer is composed of 250 nm of Si on top 3 µm of buried oxide (BOX) on a 650 µm thick Si base.

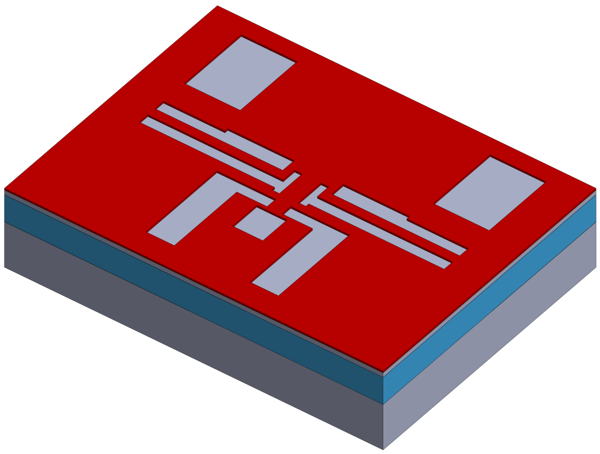

Step 1: 300 nm bilayer PMMA deposition is made, the contact pads and electrical connection guides are patterned with electron beam lithography (EBL).

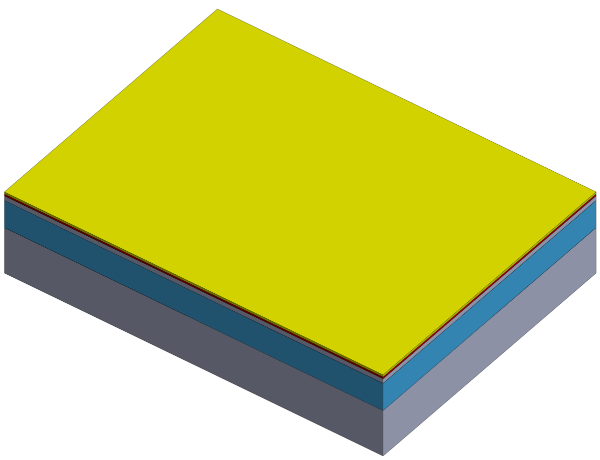

Step 2: 120 nm of Au deposition is made by thermal evaporator.

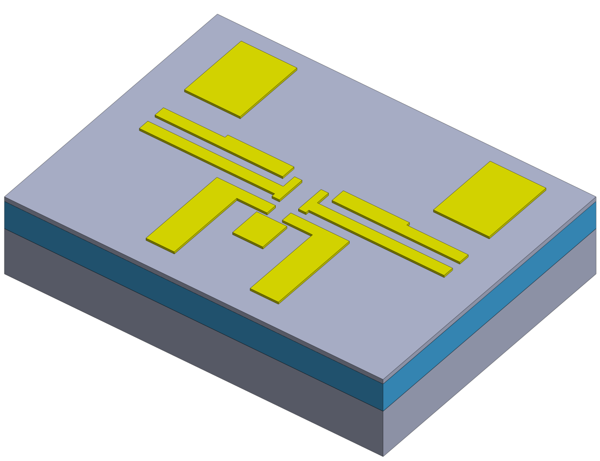

Step 3: Device is left in acetone bath for lift off at least 12 hours.

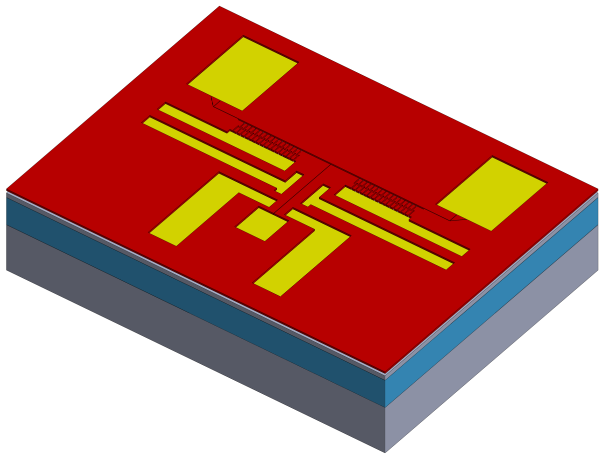

Step 4: 300 nm bi-layer PMMA deposition is made, contact pads, electrical connection guides, beam and comb drives are patterned with EBL.

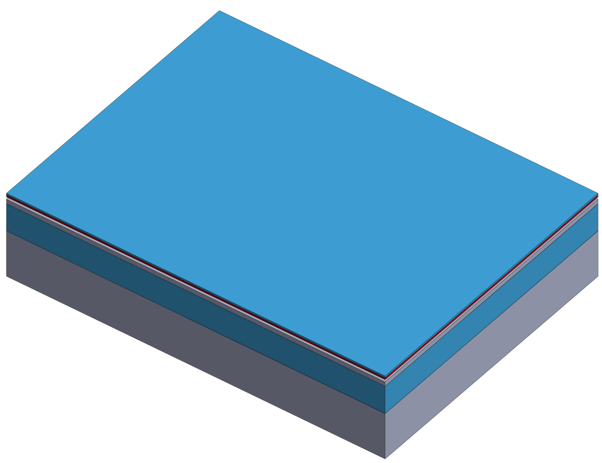

Step 5: 100 nm of SiO_2 is deposited with electron beam evaporator.

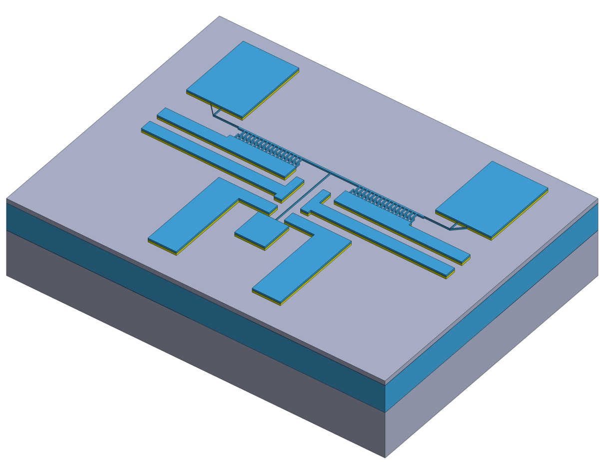

Step 6: The device is left in acetone bath for at least 12 hours for lift off process.

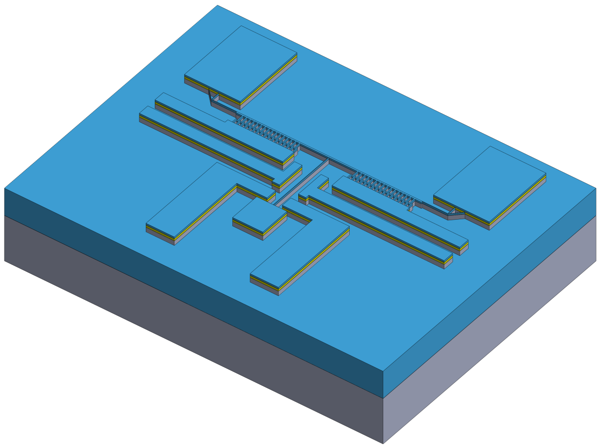

Step 7: Anisotropic dry etching is performed by inductively coupled plasma (ICP) using Cl_2. During this step SiO_2 protects the silicon beneath it from being etched.

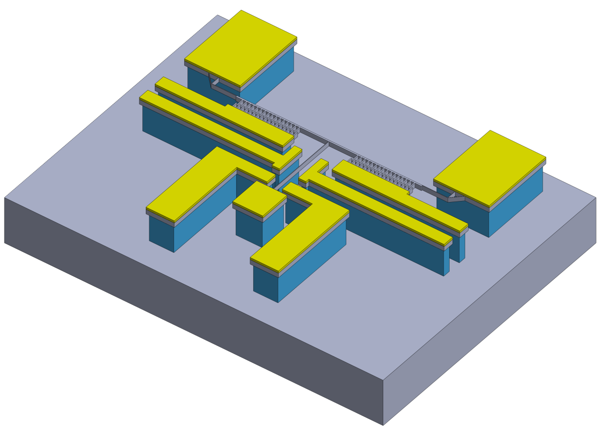

Step 8 (Final Step): Isotropic dry etching with hydrofluoric (HF) vapor is performed to get rid of the SiO_2 mask and the BOX layer, which results as the suspended structure.

Previously, at the step 4, EBL pattern was only made for the beam and the comb drive actuators. Both the contact pads and the electrical guides were not covered with SiO_2. To protect golden layers from etching at the ICP process (Step 7), mask is changed such that all the functional parts of the device are covered with SiO2.

Chapter 3

Ultrafast Measurement of Buckling Motion with SEM Line Mode

Controlling the amplitude and direction of the buckling at nano scale without the generation of the significant heat pave the way for novel actuation and sensing applications. Sensing the buckling motion at nano scale while simultaneously controlling the motion opens the path to understand full buckling behavior starting from unbuckled position to post buckling region.

3.1 SEM Full Frame Mode and Line Mode

Most common way to visualize a sample with the SEM is using the full frame mode where electrons start a scanning cycle from left to right, starting from the top and moving to a lower line subsequently after each cycle finishes. When the lowest line is reached, it returns to the very first position where the scan was initiated (Figure 3.1 a). SEM also employs line mode and spot mode in addition to full frame mode. At the former, only a single line of choice is scanned and after one cycle finishes, electron line starts the new cycle from the same line rather than moving to a bottom line (Figure 3.1 b). At the latter, a circular area of choice is scanned. For the context of this thesis, full frame and line mode operations will be relevant.

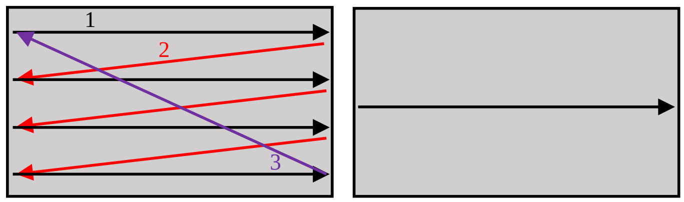

Figure 3.1: Demonstration of full frame (a) and line mode (b) operations.

Line mode is used as a tool to differentiate the side gates and the beam from their surroundings. Starting from the left, line detects the drop from side gate to bottom Si layer. Then as it goes through the beam, a sudden jump and drop is observed. Finally, a jump is observed once more as line moves from bottom Si layer to the right side gate. Adjusting the voltage and current values of the electron gun plays a critical role to observe the side gates and the beam from their surroundings.

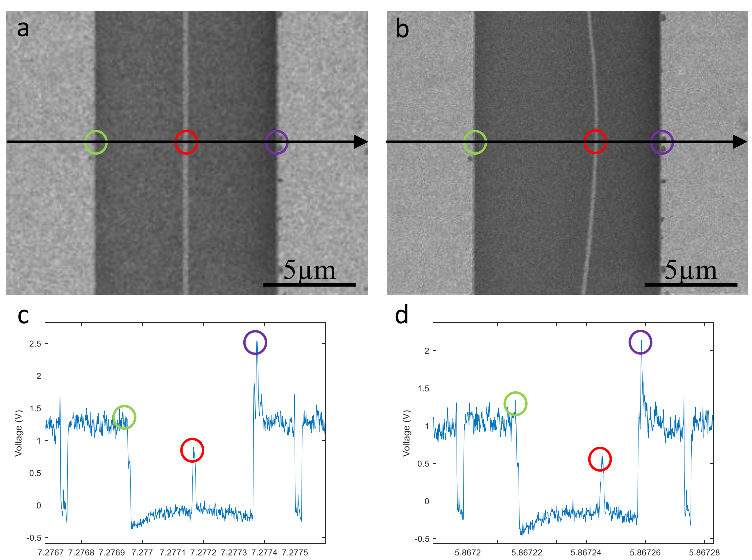

Figure 3.2: Line mode operation illustrated in SEM for unbuckled (a) and buckled (b) beam and corresponding raw data of unbuckled (c) and buckled (d) beam from the secondary electron output of SEM.

3.2 Setup and Experimentation

Experiments are conducted inside an SEM chamber where the chip is placed to a PCB. Inside the chamber, electrical connections to the PCB are made by SMA connectors. Cables extend from chamber to outside by electrical feedthroughs and have BNC connectors for connecting to a voltage supply. Throughout the experiments, Rohde Schwarz HMP 2030 is used for applying voltage to the buckling device. HMP 2030 has 3 channels, which can be controlled separately or together and extending to maximum of 32.050 V. For the sake of all buckling experiments in this thesis, the beam, hence the movable combs, are kept at ground level. To overcome the critical buckling force a voltage more than one channel can support should be applied. Thus, channels 1 and 2 are connected in series and a combined voltage is applied to the stationary combs. Voltage from channel 3 is applied either to the left or right side gate. The data for secondary electrons are extracted from the SEM by a BNC cable from port X6 of SEM. A BNC cable is connected to Compact RIO for data acquisition with a rate of 200×10^3 samples per second. Electron gun voltage is selected as 5kV, 10kV or 15kV.

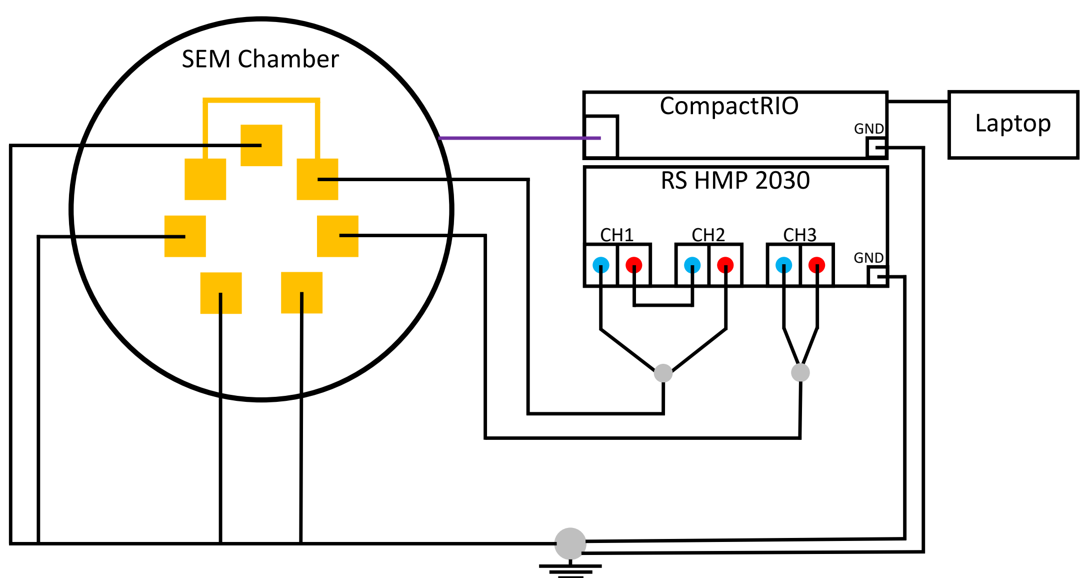

Figure 3.3: Experiment setup. Purple line represents the BNC cable for collecting secondary electrons.

Preparation for experiment includes the adjustment of the line scan period, full frame window and electron gun voltage. Line scan period is chosen as 30 µs. At the beginning of the experiment full frame mode is shrunken so that it only contains a small portion of the two side gates and the beam. Even though smaller portion of the full frame is recorded during the experiment, only one specific line is analyzed for position measurement. That line is chosen based on the transition point which is indicated by the white line at Figure 3.4.

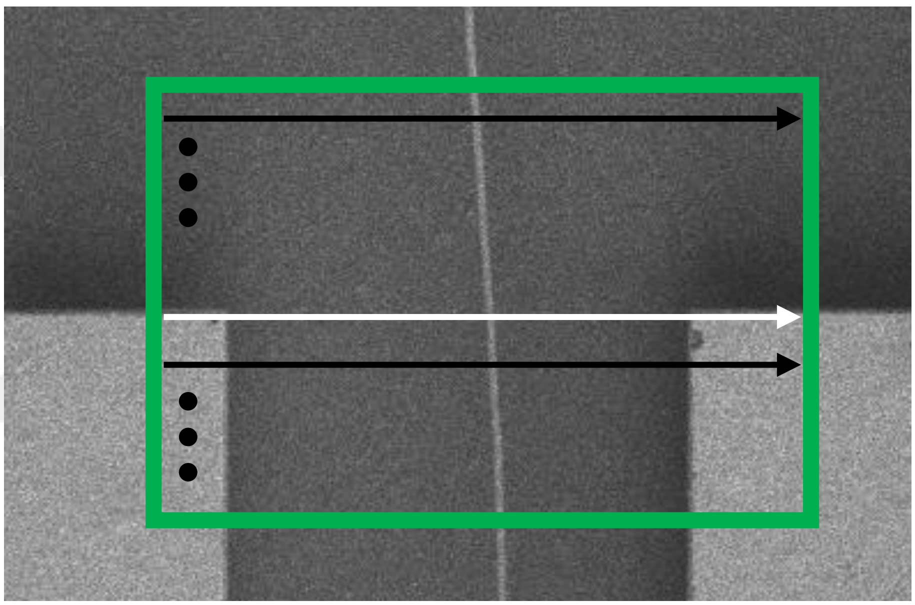

Figure 3.4: Line mode operation illustrated in portion of full frame (green rectangle), starting from top position to bottom. Only the data points containing white line is analyzed for the sake of position measurements ensuring that same point at the beam is investigated.

Transition point is reached when the scanning line gets in range of the side gates which is detected from the secondary electron data (Figure 3.5). The reason for using the shrunken full frame mode is to guarantee that the same line thus the same point at the beam is analyzed, since applying voltage to the buckling device causes a shift in the SEM image.

After preparation step is done and shrunken full frame window is adjusted, data is acquired from the unbuckled beam with no side gate voltage applied, to take the position of the unbuckled beam as the reference point. Then, the side gate voltage is applied to the device. In that instant no voltage is applied to the stationary combs hence there is still no compression force present on the beam.

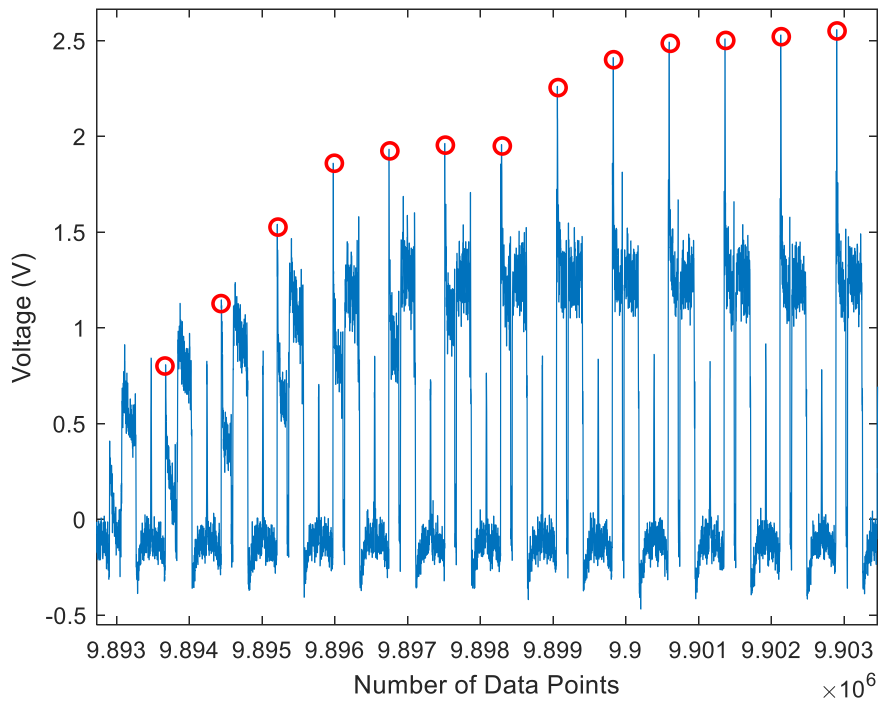

Figure 3.5: Transition point is observed as side gates stop increasing in voltage value and red dots align.

After recording the beams position at that configuration as well, stationary comb voltage applied by using the HMExplorer which is the software of Rohde-Schwarz HMP 2030. Starting from 0 V voltage value is increased to 38 V by 0.2 V steps. Before increasing the voltage to the next value, current voltage value is hold for 2.5 seconds so that couple of measurements from the same point can be taken. After the measurement is completed, starting from the unbuckled position until reaching to large deformations, beam is brought back to the unbuckled position, side gate is turned off and same procedure is applied for varying side gate voltage values.

3.3 Data Analysis and Results

A typical experiment takes around 5 minutes. With 200×10^3 samples per second data acquisition rate, we end up with approximately 60×10^6 data points. The code takes a single input from the user at the beginning for a place to start scanning. Then it detects the beam or the right side gate. After detecting one beam or side gate peak and using the periodicity, it scans the entire range of data to find the beam peak and the right side gate peak. By subtracting index values of the beam peak and the right side gate peak, the deflection amount is calculated from the reference value. Error bar is calculated by standard error of the mean with the formula:

$$\text{Standard Error} = \frac{\sigma}{\sqrt{\text{n}}} \tag{3.1}$$

where n is the number of measurements of the same point. Entire operation of the code takes less than 10 seconds for 60×10^6 data points.

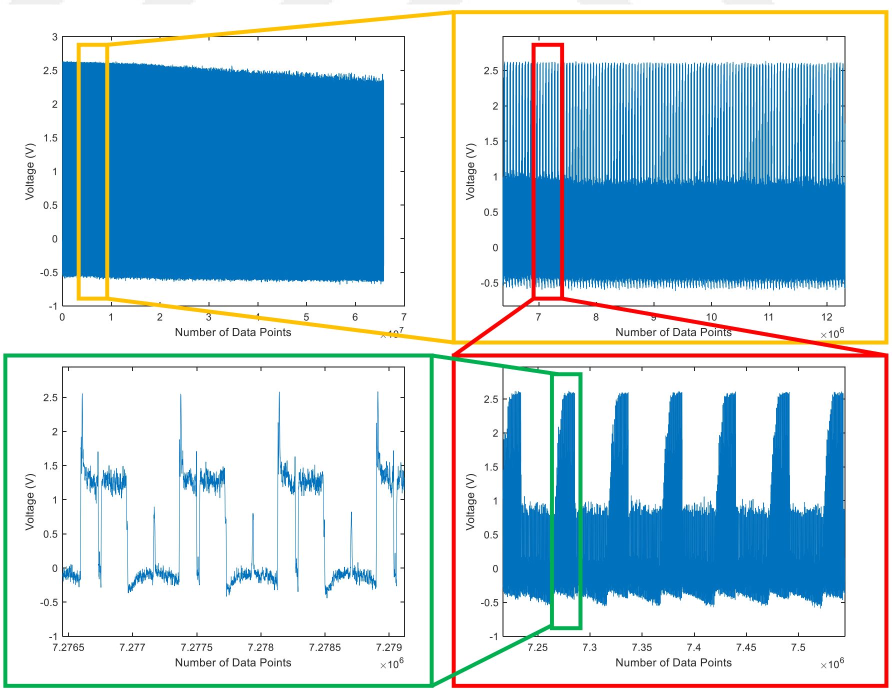

Figure 3.6: Data taken at a typical experiment and zoomed versions.

After the data processing at MATLAB, deflections as low as 15 nm were detected. Error bars having value of ±7 nm were recorded. Considering the frequency of the line mode and recorded error bars, noise floor is calculated at 38.5 pm/$\sqrt{Hz}$, which is a 250 times more improvement compared to our groups earlier work at the reference [25].

The bending caused by applying voltage only to the side gate was detected with error bars being less than the bending amount. Additionally, the inflection point where second derivative of the voltage-deflection graph becomes zero was detected. The results obtained, can further help us to understand the stiffness behavior of nano buckling systems at post bifurcation regime with a great precision.

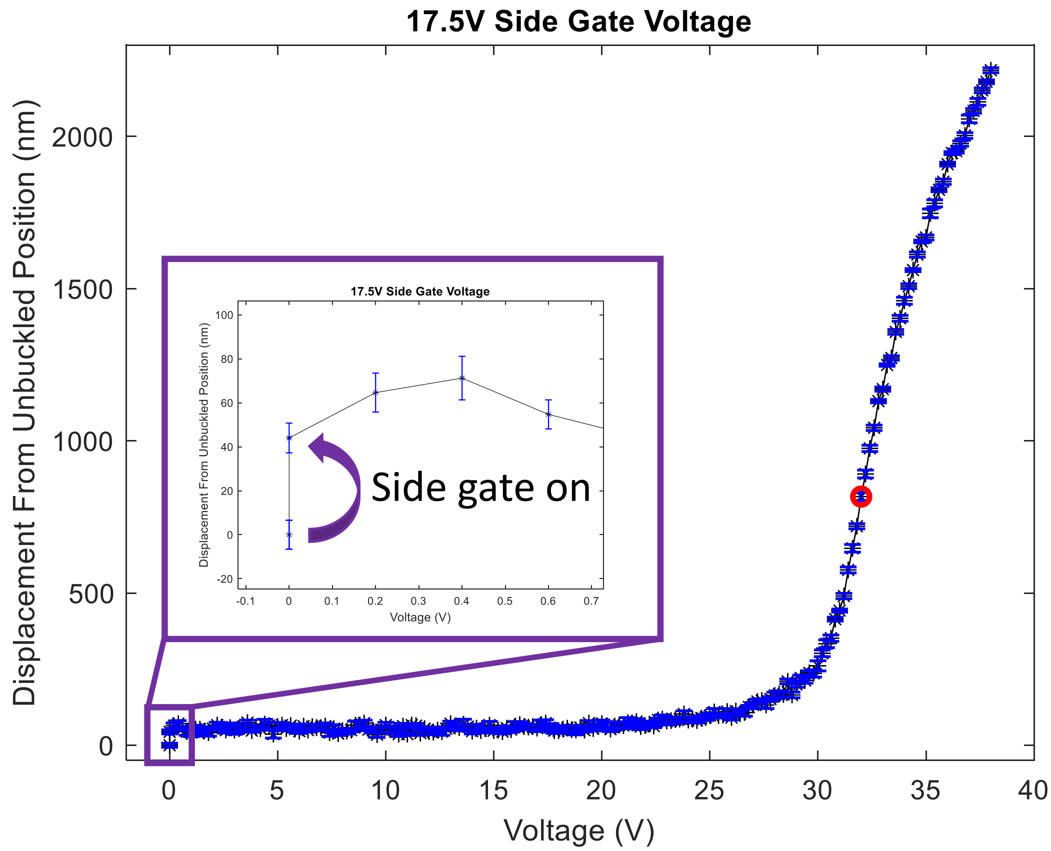

Figure 3.7: Measurement of the beam starting from unbuckled position, reaching to large deformations at post buckling region. Sub Figure shows the effect of the side gate. Red circle is the inflection point.

By further decreasing the beam width with changing the EBL process, the effect of varying side gates was detected, in which the displacements for different voltage values were out of the range of the error bar. Figure 3.8 corresponds to the bending of the beam when side gates are turned on while no comb voltage difference, hence no compression force, is applied.

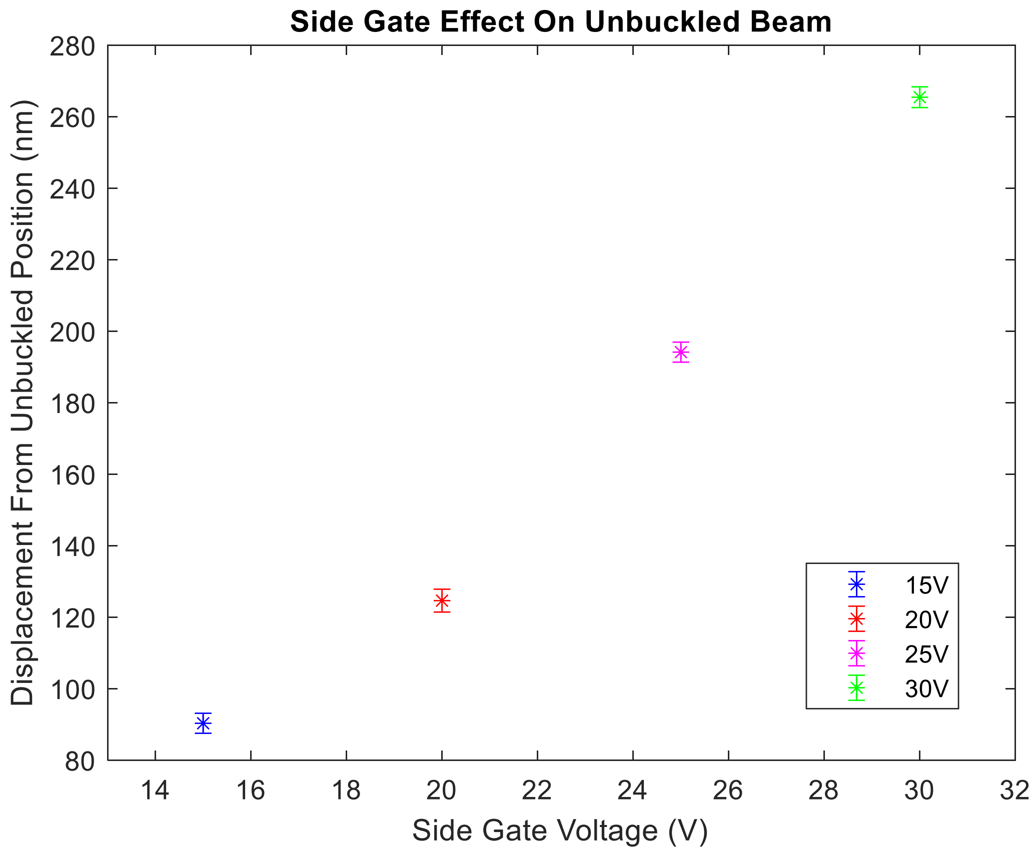

Figure 3.8: Varying side gate voltage effects on unbuckled beam.

Chapter 4

Forced Double Well Oscillator with Nanomechanical Buckling

4.1 Bifurcation and Double Well Analogy

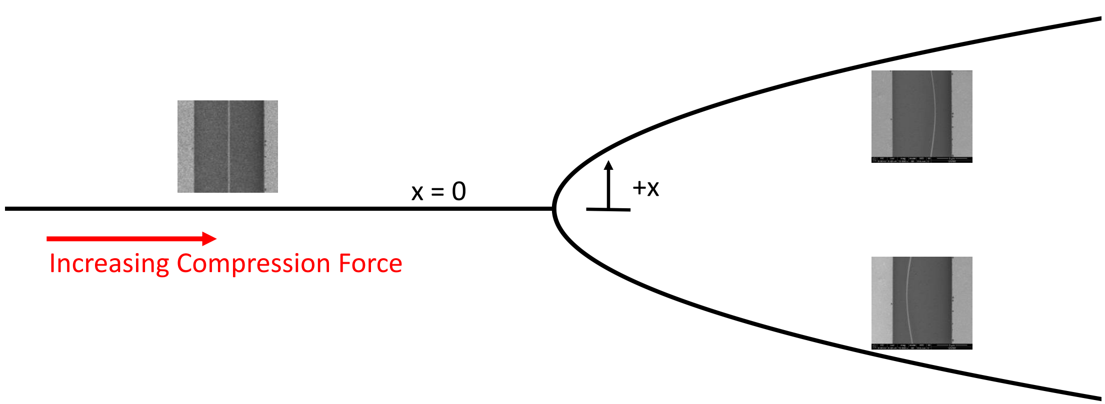

Figure 4.1: Pitchfork bifurcation and corresponding states of the beam.

Buckling is a symmetric physical phenomena having spatial symmetry between left and right states. Until the compression force applied reaches to the critical buckling force, beam is at the stable position at x = 0. If the compression force is increased further, position at x = 0 becomes unstable and two symmetric stable solutions arise. Those solutions physically correspond to beam buckling either to the left or to the right (Figure 4.1).

The post buckling behavior of the beam can be modeled with the double well potential. Unstable solution corresponds to the middle part of the well and two stable solutions can be expressed as the left and right buckled states having absolute minimum potential value.

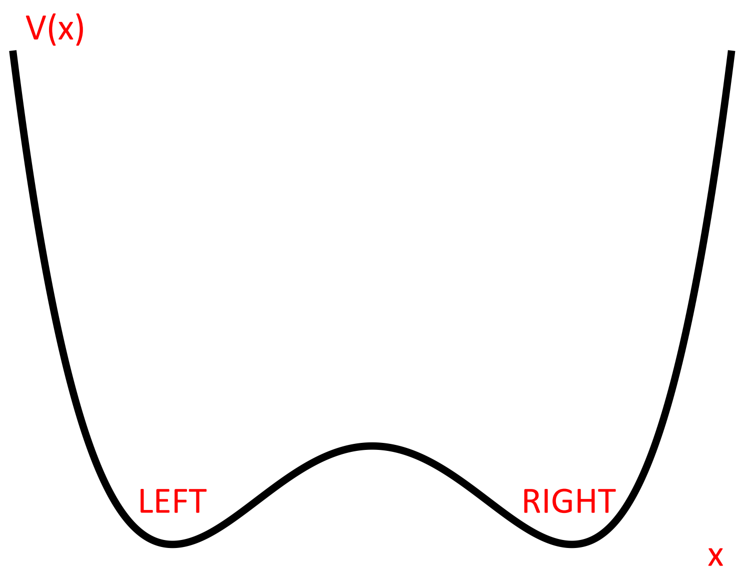

Figure 4.2: Double potential well and corresponding buckling states.

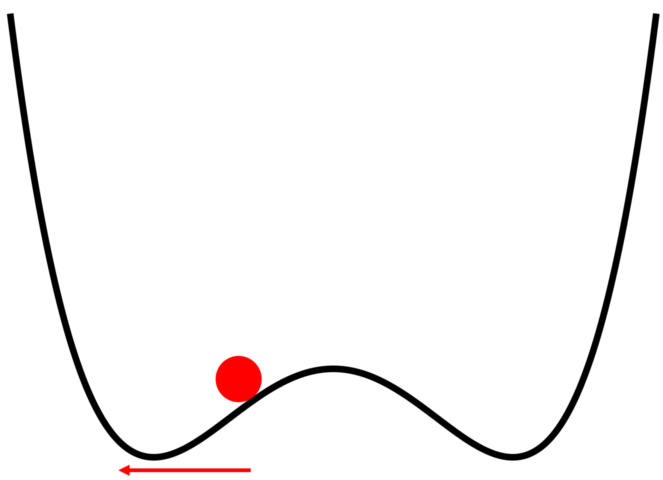

Consider that a ball placed to a well having random initial conditions.

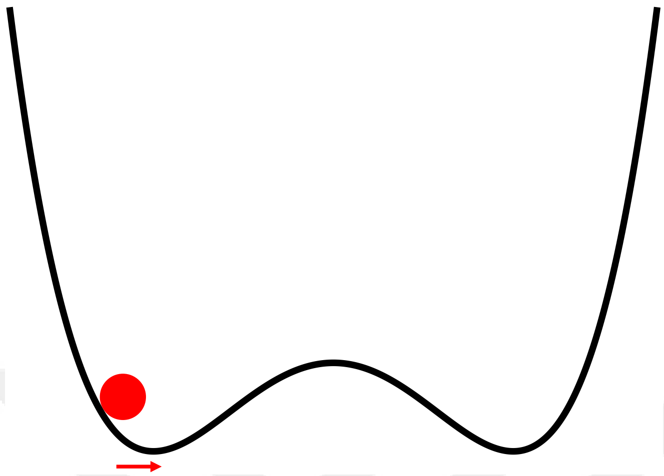

With the existence of damping its velocity will be decreasing eventually leading ball to settling to one of the wells.

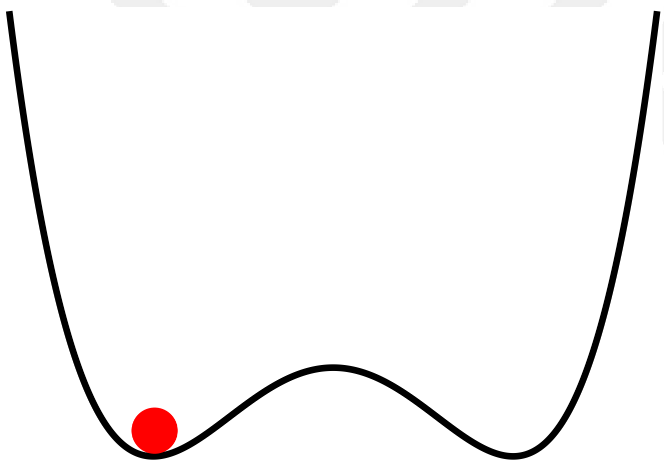

The choice of the well (left or right) depends on the damping constant and the initial conditions (position and velocity).

After the ball has settled to one of the stable configurations, it is possible to drive the ball out of the equilibrium position by shaking the system which can be modeled by the dimensionless equation [44].

$$\ddot{x} + \delta\dot{x} - x + x^3 = F\cos(\omega t) \tag{4.1}$$

where δ is the damping constant and is greater than zero, F is the forcing strength and w is the forcing frequency. The frequency of the shaking effect will be fixed, and amplitude dependence of the trajectories will be investigated. Depending on the amplitude of the shaking three different trajectories could be observed. If the shaking amplitude is small, the ball will oscillate at one of the wells and if the shaking amplitude is large enough it will oscillate back and forth between two wells. Both of those motions are predictable meaning that they do not have a huge dependence on the initial conditions and their trajectory can be represented as a periodic function after the transient effect of initial conditions disappear.

The third trajectory occurs when shaking force amplitude is in between the first two cases. A chaotic trajectory arises which depends extremely on the initial conditions and which has a non-periodic motion during its trajectory.

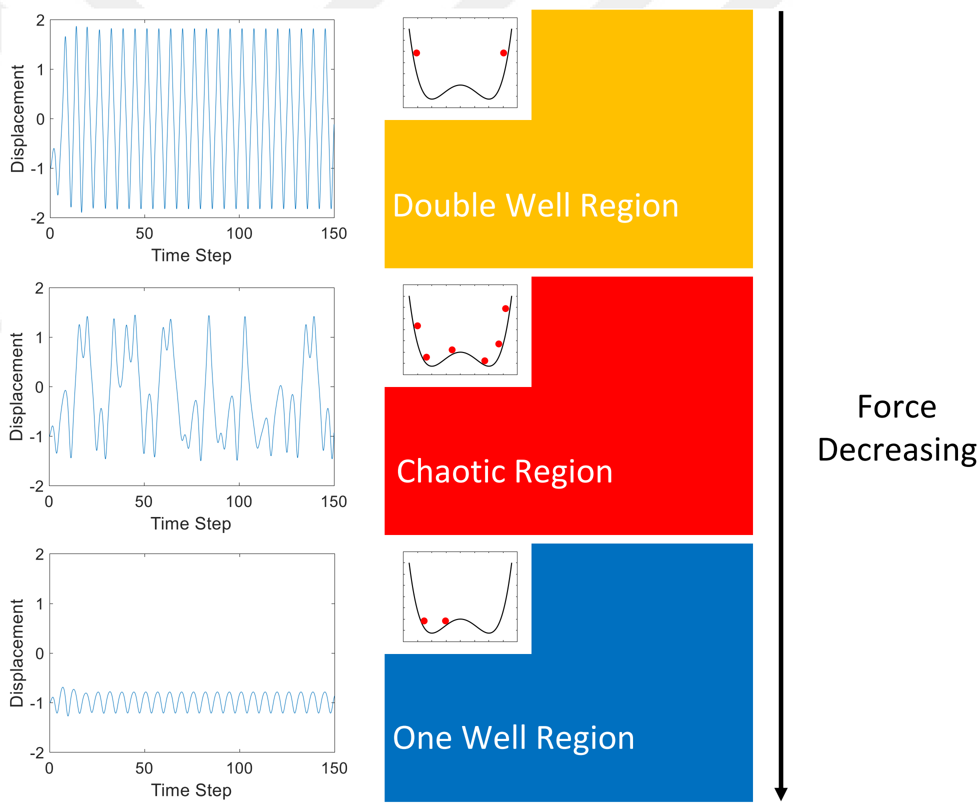

Figure 4.3: 3 regions with the changing forcing amplitude.

Recalling our buckling system, it is possible to adjust potential well depth by increasing/decreasing the comb voltage difference at the post buckling state and apply a periodic force from one of the side gate pairs. The depth of the well increases with the increasing comb voltage difference and a periodic function can be directly applied to the side gates by a function generator.

4.2 Setup and Experimentation

The experiments are conducted inside the SEM chamber. Buckling device is placed to a PCB and wirebond connections are made to apply voltage and signal to the device. PCB has SMA connections which extend from inside the chamber to outside of the chamber by electrical feedthroughs. During the experiment, a DC voltage is applied to the stationary combs, the movable combs and bottom pair of side gates are at the ground level and an AC voltage is applied to the top pair of side gates. DC voltage is applied by Rohde Schwarz HMP 2030 by combining channels 1 and 2 to overcome the critical buckling force. AC voltage is applied by Keysight 33600A Series waveform generator and a custom built amplifier is used to amplify the AC voltage amplitude by 6.5 times. Throughout the experiments AC voltage frequency of 0.55 Hz is chosen. Two channels of the signal generator are adjusted so that a 180 degrees out of phase voltage could be applied to the side gates, that is, when one side gate has the highest voltage value, the other one has the lowest value and vice versa.

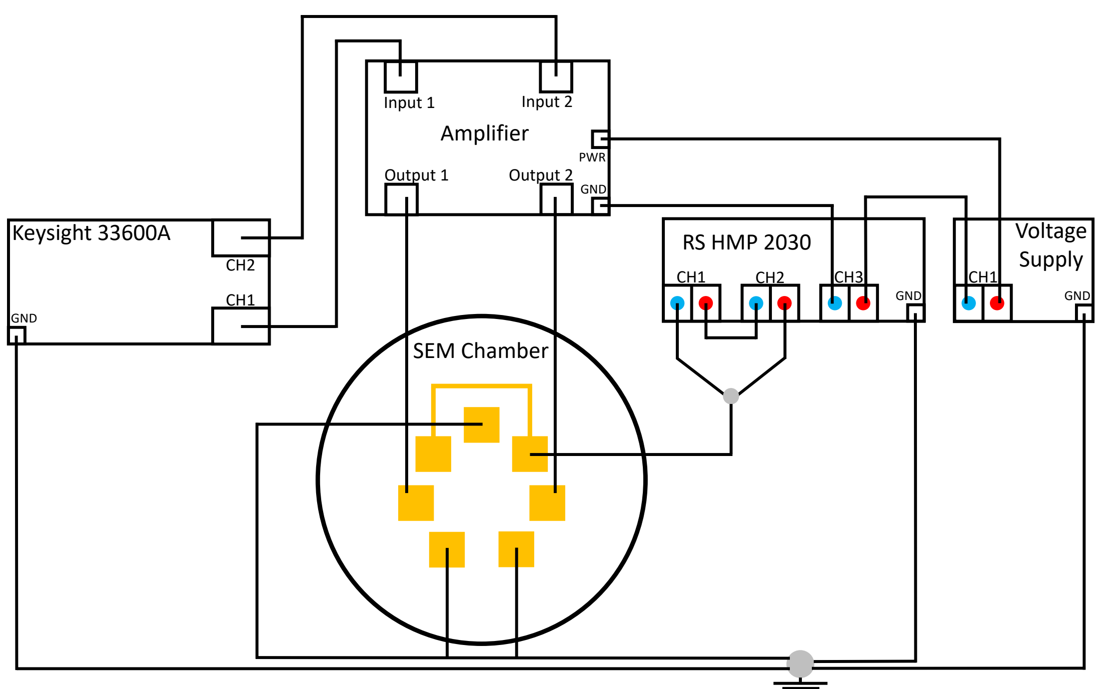

Figure 4.4: Experiment setup.

After placing the device inside the chamber and making electrical connections, a contrast and brightness adjustment is made such that the entire buckling device is brighter than the surroundings. The necessity of this step is to get a high contrast image for image processing which will be explained in detail at the section 4.3. After the contrast and brightness adjustments, voltage is applied to the stationary combs to ensure buckling amount of approximately 1.5 µm so that double well oscillations are easily detectable. Then, the channels of the signal generator are turned on to apply AC voltage to the side gates. A voltage scan is performed from large voltages to low voltages by steps of 0.02 V from the signal generator. This corresponds to 130 mV after the signal passes through the amplifier. Voltage values in which the beam oscillates between both wells are preferred in the beginning of the experiment to prevent biased buckling to either of the wells.

4.3 Data Analysis and Results

Experiments are recorded as a high quality movie from start to the end with rate of 10 frames per second. High blur is generated due to voltage oscillations so only steady frames are analyzed which are passed through a salt and pepper filter to get rid of background noise. After the filtering operation, the image is converted to a binary image in which contrast difference becomes significant for smoother transitions.

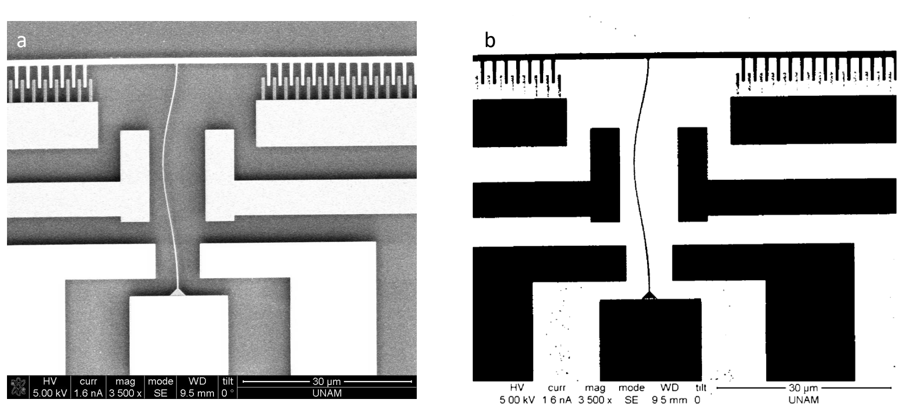

Figure 4.5: Original device image (a) and binary device image (b).

The edge of the top right side gate is chosen as a reference point by 2 step white to black and black to white transition, and from that reference point beams position is calculated by counting number of pixels. The code uses advantage of black to white and white to black transitions to detect the reference point and to calculate the position of the beam at each individual frame.

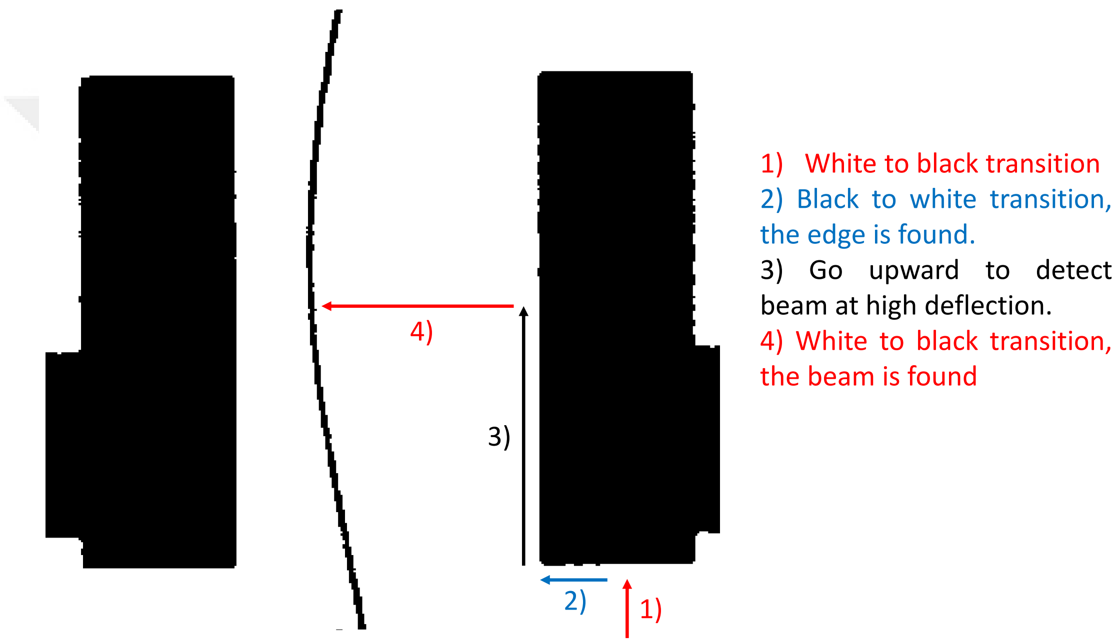

Figure 4.6: Visualized operation of the code.

The Figure 4.7 was conducted where comb drive voltage difference was 35.5 V and the beam was initially buckled to right. Left deflections are recorded as negative displacement values while right deflections are recorded as positive displacement values. 0 corresponds to the position of the beam when it is at unbuckled state. One well and double well oscillations are easily generated as the former only need a small voltage amplitude and latter need a large voltage amplitude.

The chaotic state(s) however, need to be precisely scanned throughout the experiments. An evidence of a chaotic trajectory found in the same experiment, is shown at Figure 4.7. Please note that since the beam was initially buckled to the right in that experiment, it has higher tendency to be at the right well, hence one well oscillations at the left well were not observed.

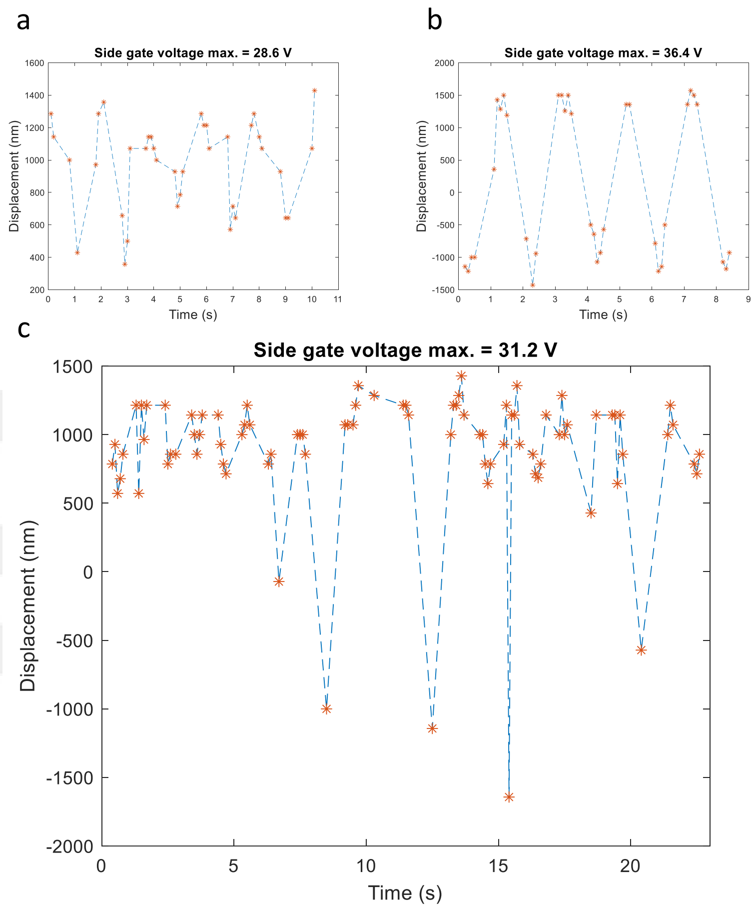

Figure 4.7: One well (a), double well (b) oscillations and chaotic trajectory (c).

At a seperate experiment, 38 V comb voltage difference is applied to comb drive actuators. As a starting point, an educated guess is made for the voltage value of the side gate for achieving a chaotic trajectory. It is particularly important to achieve chaotic region at the very beginning of the experiment before a beam bias to one of the wells occurs. Beam motion was observed in initially at right well, passing to double well and finally converging to left well (Figure 4.8).

Then, side gate voltages are applied starting from high voltages (ensuring that double well oscillation occurs) to low voltages, when one set is completed, same procedure is applied, starting all over. Starting with a 25.87 V side gate voltage amplitude, an interesting pattern was observed with decreasing voltage.

Motion which was initiated at one well then converged to double well. This

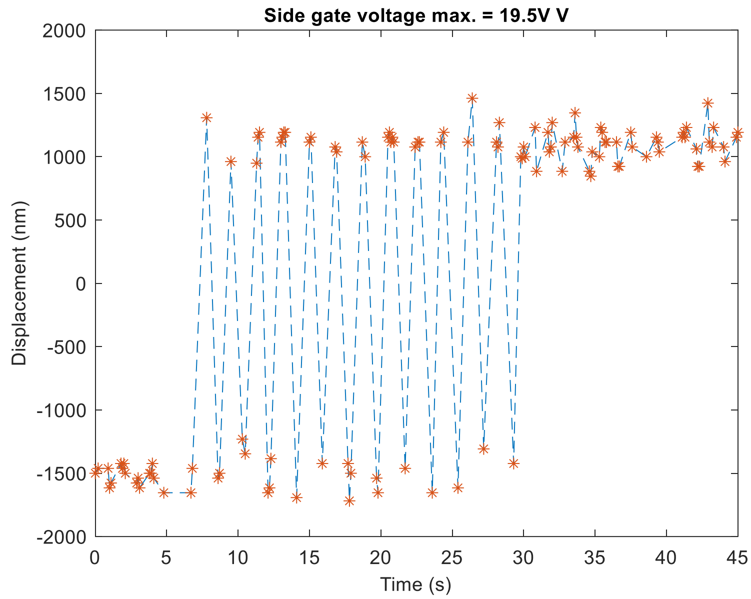

Figure 4.8: Chaotic trajectory.

should not be thought as transient chaos in which the motion starts in chaotic region and then settles down to one of the stable states. Our system initially starts its motion oscillating at left well, then converges to double well, from now on referred as transition region. Recalling that voltage was decreased, before system reaches that point in Figure 4.9 it was doing a purely double well motion. System tries to resist leaving the double well motion as voltage is decreased.

Similar behavior was also seen at other voltages values at Figure 4.10 (a), (b) and (c). Additionally, an evidence of chaotic region (d) and one well oscillation (e) was observed as well. Analyses of Figures 4.9 and 4.10 suggest us that transition region is present at our nanomechanical buckling platforms which exists in somewhere between double well oscillation region. Please note that the initial one well motion tendency at Figure 4.10 (c) is neglected since it occurred at the moment when waveform generator was turned on.

Existence of transition region could be explained by the dynamic shape change on the double well potential during the experiments. Similar to the relation between initial buckling direction and systems choice of stable well position, system tries maintaining previous state of trajectory, until it reaches a point where it is

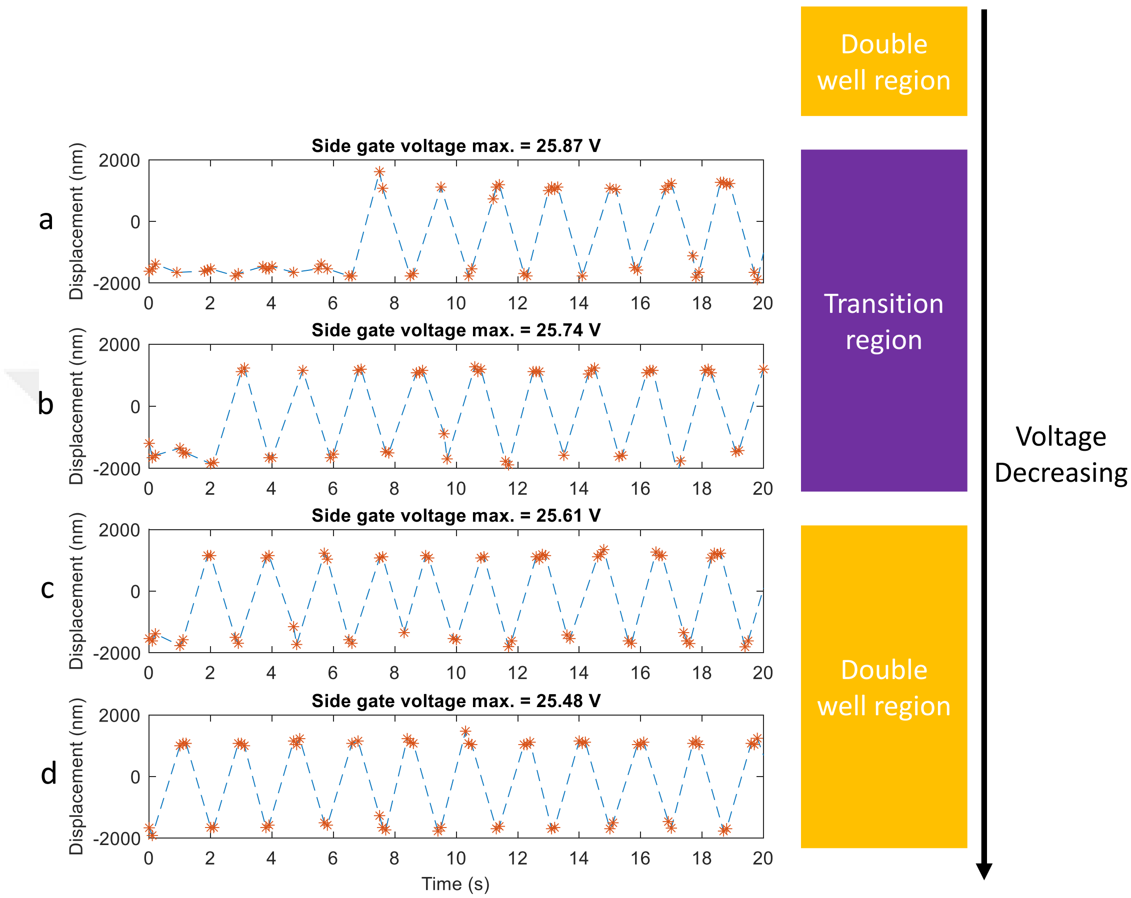

Figure 4.9: Transition region existing between double well regions. Existence of upper double well region is known intuitively since applying voltage high enough will generate that motion for sure.

no longer possible to maintain that type of trajectory with decreasing voltage.

Additionally, in the same time lapse for different voltage values, the percentage of the beam doing double well motion decreases with increasing voltage (Figure 4.11). Vertical axis corresponds to the probability of double well oscillation during the entire time lapse of the trajectory. It is calculated by counting the double well trajectories within the period of 1.81 seconds. Horizontal axis refers to the side gate values when they have their maximum value. The "V" shape at the Figure 4.11 (b) exists due to the transition region where double well oscillation probability drops to approximately 40% from 100%. The "V" shape also exists at Figure 4.11 (a) outside the region of the graph since applying voltage high

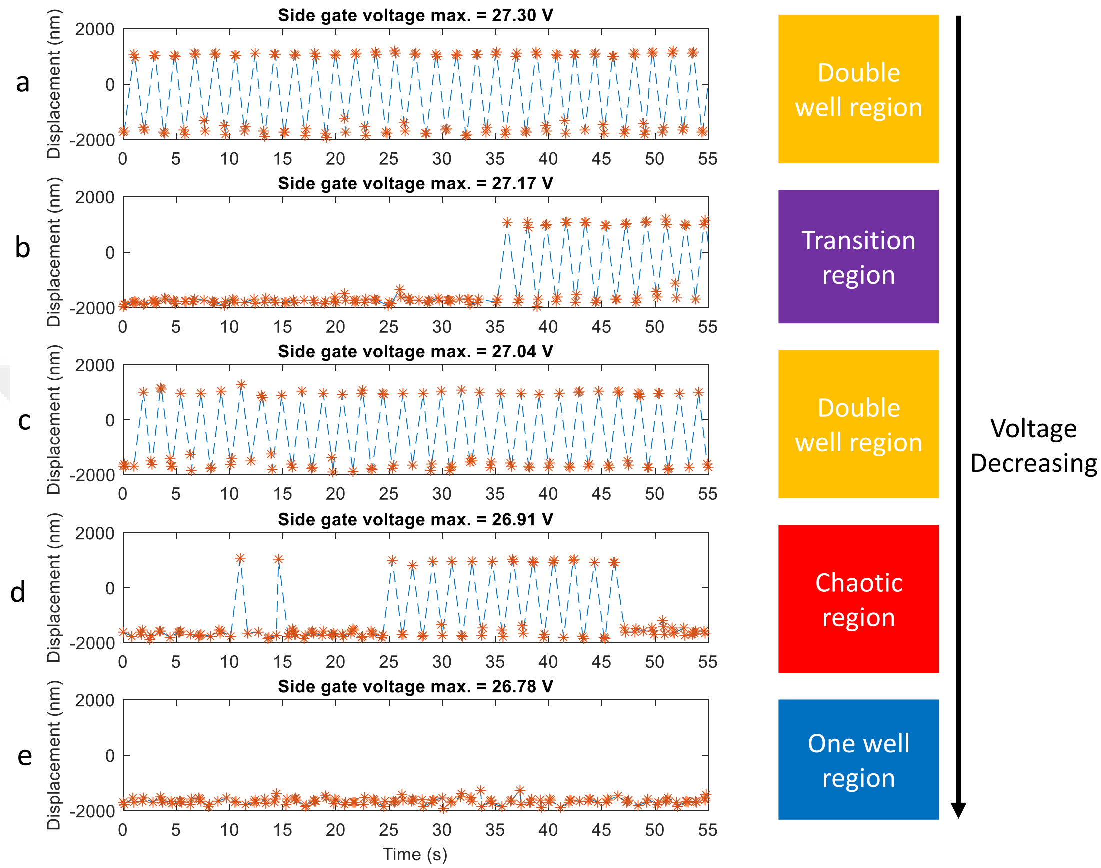

Figure 4.10: Double well, transition, chaotic and one well region all seen at narrow range voltage scan.

enough to side gates will be initiating double well oscillations for sure.

The transition region could be thought as an additional trajectory option while its sub trajectories, one well and double well oscillations, are well defined, its transition from one trajectory to the other does not seem fitting to simple rules. That characteristic of it opens avenues for those systems to be used in complex computation applications such as random number generators and data security protocols.

Moreover, observing chaotic regions experimentally for narrower side voltage steps and for different well depths, which are adjusted by comb drive actuators, is important to fully observe chaotic regime at nanomechanical buckling platforms. Additionally, effect of the plastic deformation should be considered to best operate

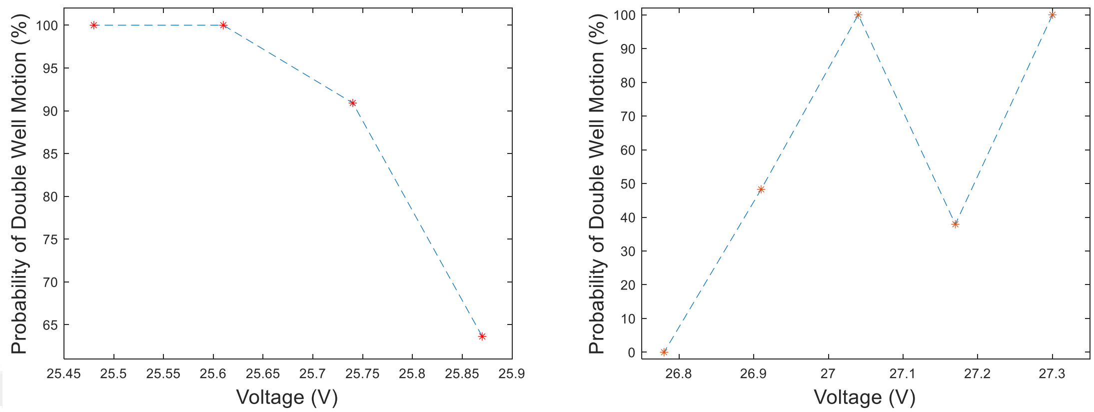

Figure 4.11: Probability of double well oscillation at full time lapse of motion for Figures 4.9 and 4.10.

those devices in chaotic and/or transition regions during the device operation.

Chapter 5

Critical Coupling at Ring/Racetrack Resonators for NEMS Measurements

5.1 Ring Resonator Model

Considering the model with one ring resonator and one waveguide the equations for the power transmission will be derived based on Yariv [45]. I_1, I_2, T_1 and T_2 are normalized amplitudes. Light entering from I_1 could follow variety of paths including total transmission to T_1, total coupling to ring or combination of two options, theoretically (Figure 5.1).

Assuming that waves travel in one direction with no reflection taking place and powers entering and leaving the coupling region, indicated by red box, are equal, coupling can be expressed by two constants c and t, and the interaction can be expressed with the matrix:

$$\begin{pmatrix} T_1 \\ T_2 \end{pmatrix} = \begin{pmatrix} t & c \\ -c^* & t^* \end{pmatrix} \begin{pmatrix} I_1 \\ I_2 \end{pmatrix} \tag{5.1}$$

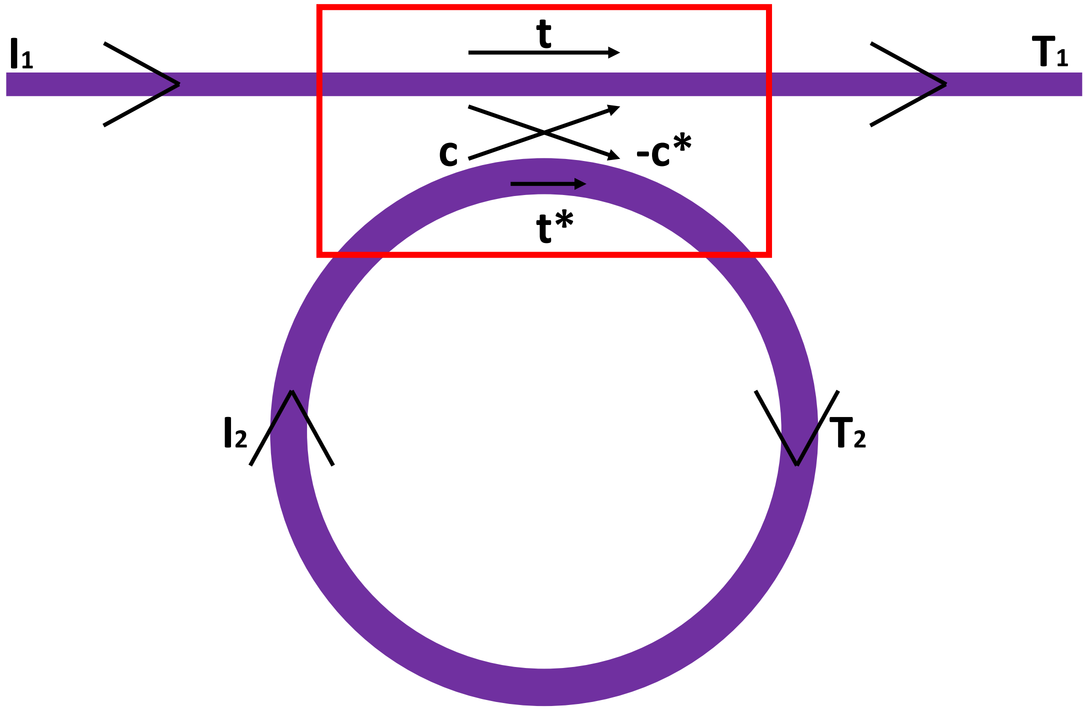

Figure 5.1: Model of the integrated optical device.

and the coupling parameters have the relation:

$$|c^2| + |t^2| = 1 \tag{5.2}$$

therefore, we get the equations:

$$\begin{aligned} T_1 &= tI_1 + cI_2 \\ T_2 &= -c^*I_1 + t^*I_2 \end{aligned} \tag{5.3}$$

The * corresponds to the complex conjugate operation. With a circular trip on the ring we have:

$$I_2 = \alpha e^{j\theta} T_2 \tag{5.4}$$

With α and θ being the loss coefficient of the ring and the phase shift at each circulation, respectively. Taking I_1 as 1 for simplification and using equations 5.3 and 5.4 T_2, I_2 and T_1 can be expressed as:

$$T_2 = \frac{-c^*}{1 - \alpha t^* e^{j\theta}} \tag{5.5}$$

$$I_2 = \frac{\alpha\,(-c^*)}{e^{-j\theta} - \alpha t^*} \tag{5.6}$$

$$T_1 = \frac{te^{-j\theta} - \alpha}{e^{-j\theta} - \alpha t^*} \tag{5.7}$$

Using amplitude power relationship, we have:

$$P_{T_1} = |T_1|^2 = \frac{|t|^2 + \alpha^2 - 2\alpha|t|\cos(\psi)}{1 + \alpha^2|t|^2 - 2\alpha|t|\cos(\psi)} \tag{5.8}$$

$$P_{I_2} = |I_2|^2 = \frac{\alpha^2(1 - |t|^2)}{1 + \alpha^2|t|^2 - 2\alpha|t|\cos(\psi)} \tag{5.9}$$

where, ψ results from both phase shifts due to the ring and the coupler. At resonance,

$$\psi = 2\pi m \tag{5.10}$$

with m being an integer, following expressions are obtained:

$$P_{T_1} = \frac{(\alpha - |t|)^2}{(1 - \alpha|t|)^2} \tag{5.11}$$

$$P_{I_2} = \frac{\alpha^2\,(1 - |t|^2)}{(1 - \alpha|t|)^2} \tag{5.12}$$

When internal and coupling losses are equal, $\alpha = t$, transmitted power becomes 0, which is referred as critical coupling.

5.2 Device Architecture

A single device is composed of two grating couplers, one for input and one or output, waveguide that connects grating couplers, a ring/racetrack resonator which is not connected to the waveguide and a doubly clamped or a cantilever beam.

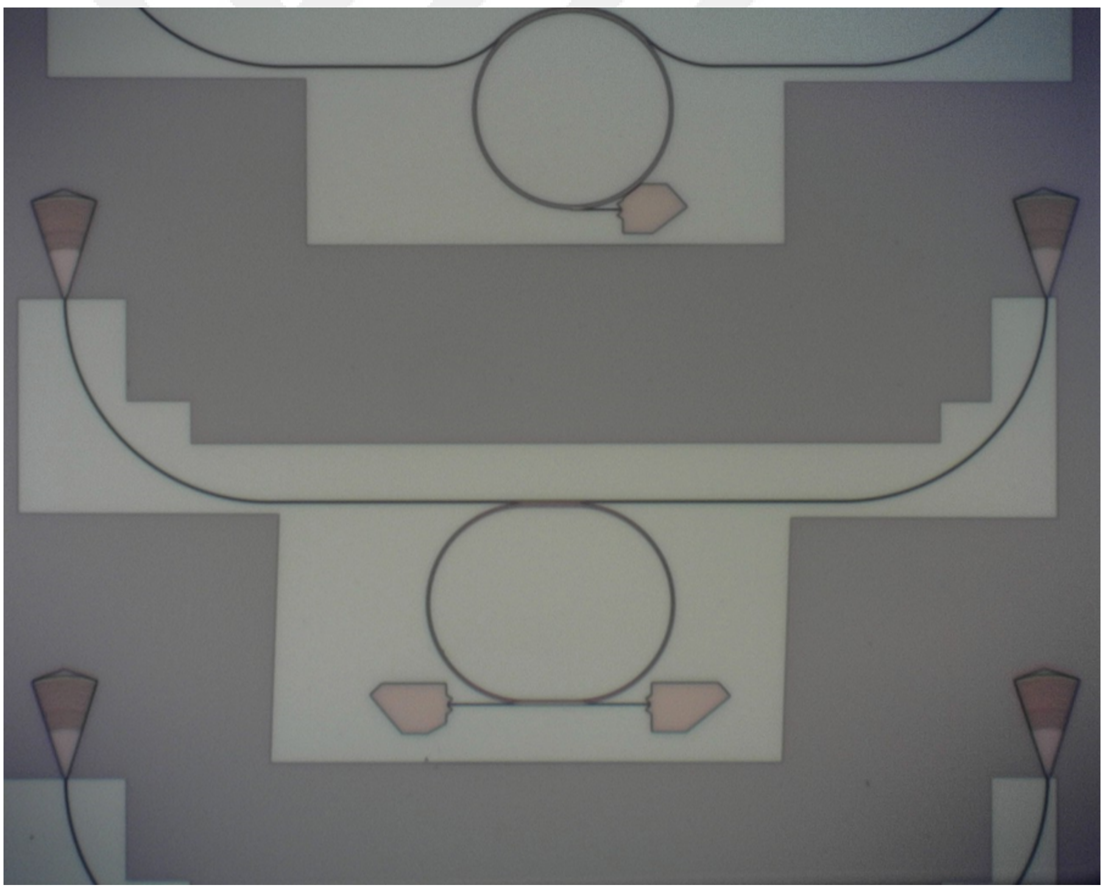

Figure 5.2: Image of a device under optical microscope.

Waveguides, ring/racetrack resonators and beams are built with 230 nm of Si_3N_4 on top of 2.5 µm of SiO_2. Grating couplers are designed to have 50 percent duty cycle with 115 nm to 230 nm thickness pattern and have a width and length of 27.25 µm to 16.12 µm respectively. Waveguides have a width of 500 nm which narrows down to 200 nm at the coupling region. Beams have varying length with 150 nm width.

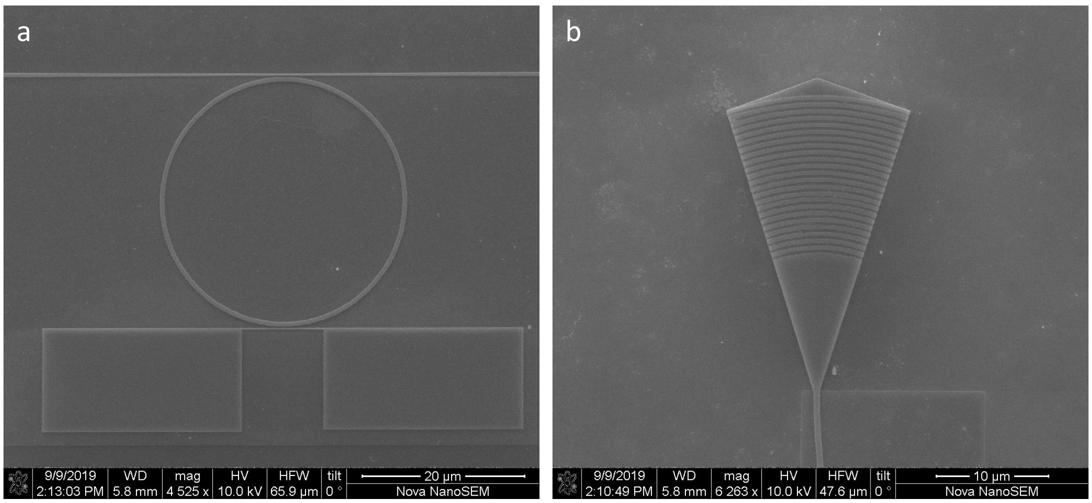

Figure 5.3: Images of a ring resonator and doubly clamped beam (a) and a grating coupler (b) under SEM.

5.3 Setup and Experimentation

Experimental setup is composed of two fibers, two 3 axis stages with a servo motor and a custom built fiber path integrated to them, optomechanical devices, a microscope and a plexiglass cage.

Single mode optical fiber supporting wavelengths 765 nm to 781 nm from Thorlabs is used.

Fibers are prepared with the guidance of the Thorlabs manual fiber preparation guide FN96A - Guide to Connectorization and Polishing of Optical Fibers. Fibers are cleaned with isopropyl alcohol first, then stripped with Jonard Tools JIC-375 from the third hole, hence glass fiber is exposed. Stripped fiber is then cleaned with isopropyl alcohol once again. The cleaned bare fiber is then cut with Thorlabs S90R Ruby DualScribe Fiber Optic Scribe for achieving a quality optical surface. After investigation of the surface, manual polishing is made with

30 µm, 6 µm, 3 µm, 1 µm polish surfaces, finalized with the polishing using 0.02 µm LFCF film.

To align fibers to grating coupler, a servo motor integrated 3 axis stage is used. While the chip remains steady, the x, y and z position of the fibers are controlled with the stage and tilt to the fiber is given by servo motors. Alignment is performed by bringing tilted fiber close to the chip surface with the z axis, until reflected light is clearly seen, which is the indicator that fiber is almost touching the surface. Then, fiber is positioned between the x and y coordinates of the grating coupler. Giving tilt to fibers is critically important to maximize the light transmission from fiber to grating couplers. Servo motors are chosen as micro version for space considerations and they are controlled with a circuit consisting of Arduino and potentiometers.

Fiber path is prepared by cutting through a 1.05 mm thick glass by a dicing saw in the cleanroom environment. The fiber path is made such that the fiber neither freely moves nor gets completely stuck at the hole. The path is connected to the shaft of the servo motor and the servo motor is connected to the 3 axis stage.

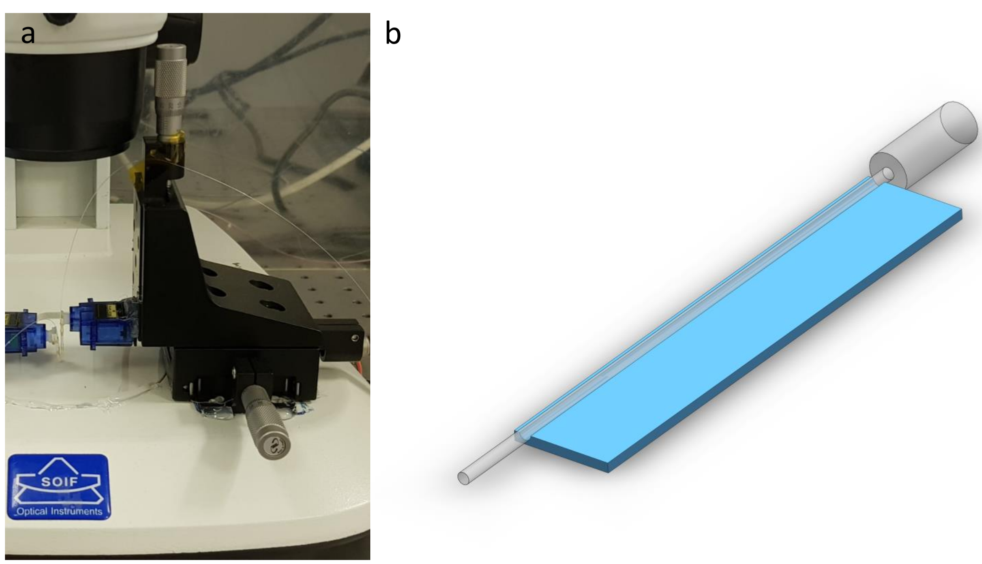

Figure 5.4: XYZ-tilt stage (a) and a model of custom built fiber holder with fiber on it (b).

Channel Depth	150 µm
Glass Thickness	1.05 mm
Tape Thickness	0.09 mm
Blade Height	0.99 mm
Feed Speed	3

Table 5.1: Parameters of dicing saw for building fiber holder.

Newport New Focus Tunable Laser TLB-6712 fine tunable laser, Thorlabs DET025AFC/M fiber optic photodetector, Stanford Research Systems Model SR560 low noise preamplifier and Keysight Agilent 34461A digital multimeter is used for experimentation.

Laser output is connected to the input fiber which aligns with the input grating coupler. The light scattered from output grating coupler is collected by the output fiber which is connected to the photodetector. Voltage output is taken from the photodetector which goes to preamplifier, then to the digital multimeter (Figure 5.5).

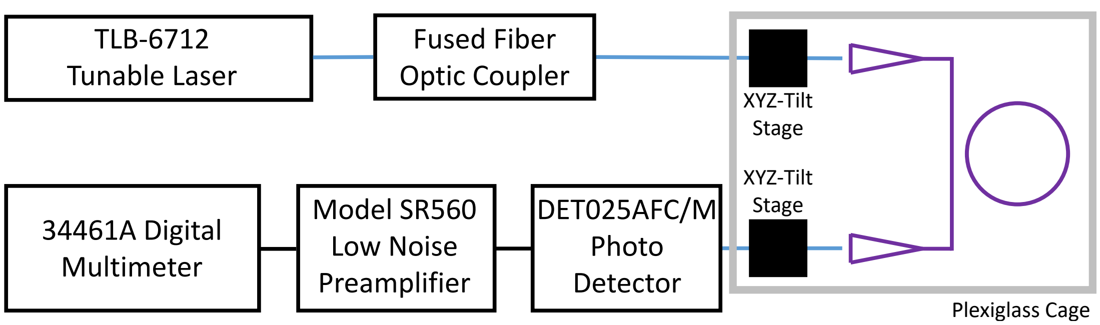

Figure 5.5: Experiment setup. Blue lines correspond to fibers.

5.4 Data Acquisition

Experiments are performed at the LabVIEW environment, using modules of the LabVIEW, Newport Tunable Laser and Keysight Digital Multimeter. For precise wavelength scan, piezo actuator inside the laser is controlled by LabVIEW.

After initialization of the instruments at the beginning of the code, laser scanning and data acquisition are done in a loop style. Starting from 765 nm wavelength of light, piezo actuator of the laser is increased by 1 %, using piezo setpoint module of the laser, which corresponds to a wavelength increase of 1.8 pm. After the light is collected from the output fiber, converted to a voltage value by the photodetector and passed through preamplifier, signal is detected with the digital multimeter and relevant wavelength and signal amplitude values are recorded. A lambda sensing operation is done by the sense lambda module of the laser to record the wavelength. This process is repeated starting from 0 % to 100 % of piezo value which corresponds to total wavelength increase of 180 pm.

After reaching to 100 %, piezo it is brought back to 0 %, again using the piezo setpoint module. The last recorded wavelength value is shown to user in the main screen for checking purposes. Then, 150 pm of wavelength increase is applied without using the piezo setpoint module but rather using the lambda setpoint and scan forward velocity modules. Recalling that piezo scan resulted as 180 pm of wavelength increase, the code ensures 30 pm of safety margin. Finally, with track lambda state user is informed about the lambda value.

Those operations are repeated until wavelength reaches to 780 nm, then the execution is automatically finished. Simplified diagram of the operation is shown at Figure 5.6, the complete LabVIEW block diagram can be found at the Appendix B.

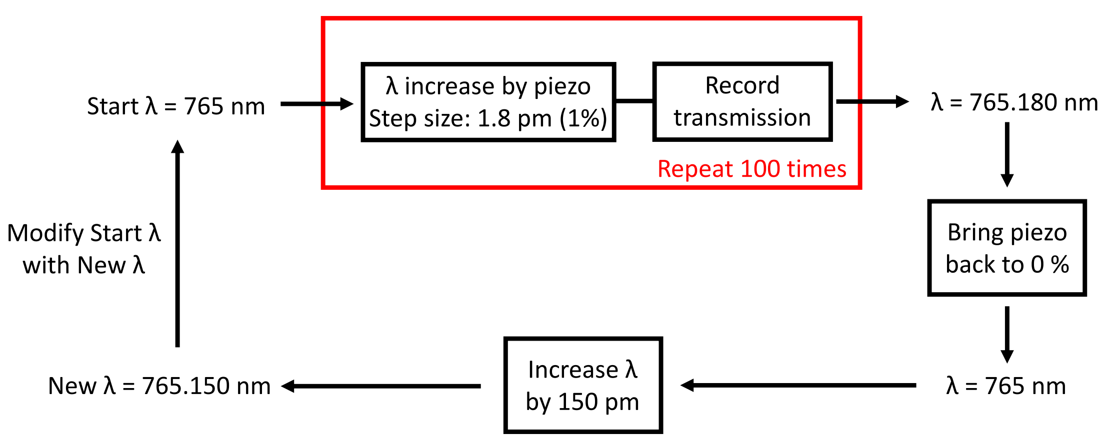

Figure 5.6: Basic diagram of the operation.

5.5 Results

Experiments took place at the room temperature and atmospheric pressure. All the no coupling, under coupling and critical coupling cases were observed during the experiments, not surprisingly, considering that 217 devices with different variations are present in a chip with dimensions of 3 mm to 10 mm. The variations include, the type of the resonator (ring or racetrack), length of the non-circular (racetrack length) part at the racetrack resonators, coupling gap and diameter of the resonator.

Figure 5.7 is a critical coupling data for a racetrack resonator having a 19 µm diameter, 5 µm racetrack length and 175 nm of coupling gap.

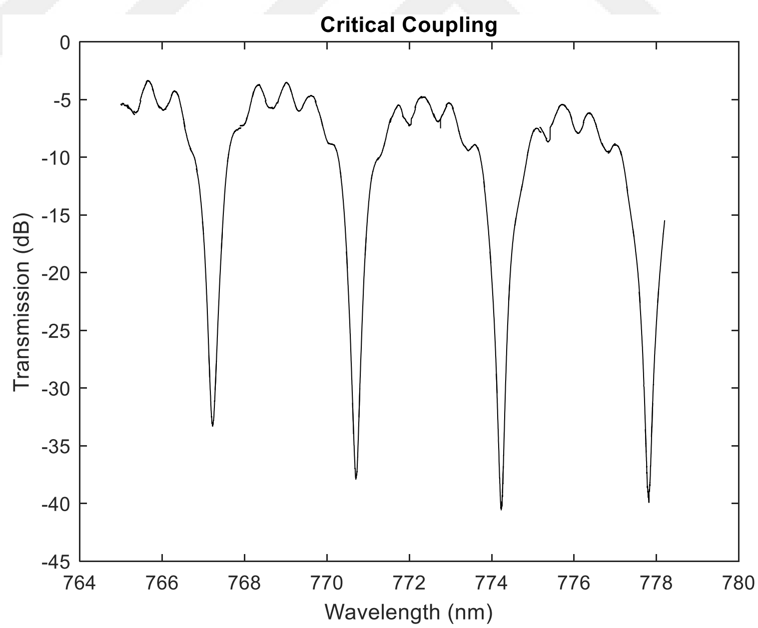

Figure 5.7: Critical coupling.

The tracks of the consecutive scans, which were explained at Section 5.4, could be observed. Purple arrows correspond to end of a scan and red arrows correspond to beginning of the following scan (Figure 5.8). Having consecutive scans overlapping each other is an indicator of a successful alignment and device design.

Figure 5.9, corresponds to an under coupled case of a racetrack resonator with 10 µm diameter, 2 µm racetrack length and 175 nm of coupling gap. Zooming to

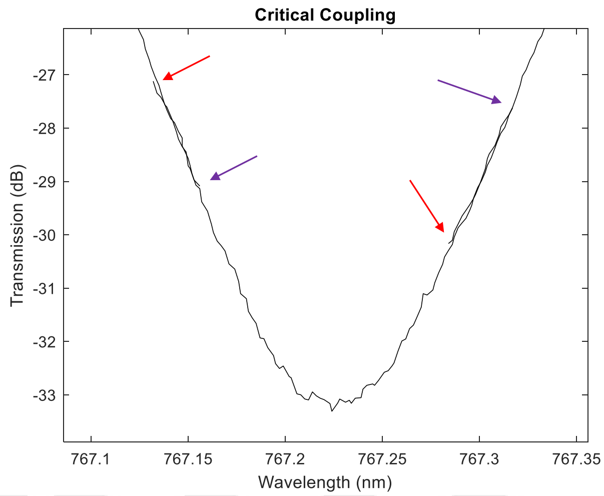

Figure 5.8: Consecutive scan steps.

the red rectangle shows an oscillation during the experimentation which could be caused by a random environmental effect. Even in that case overlapping of the consecutive scans is present.

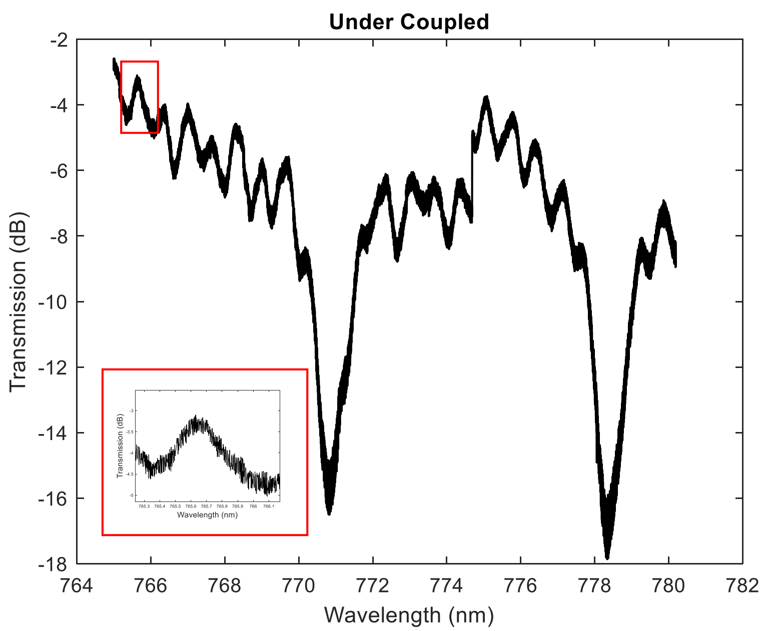

Figure 5.9: Under coupled racetrack resonator.

Chapter 6

Conclusion and Future Work

In this study, precise and low error measurement of nanomechanical buckling motion, starting from unbuckled position to large deformations at post buckling regime has been demonstrated. With the code developed error bars as low as ± 7 nm for large deformations and ± 2.8 nm for initial bending were recorded. Further, noise floor levels of 38.5 pm/$\sqrt{Hz}$ were achieved. Additionally, forced double well oscillator model was demonstrated in these platforms. Both evidence of chaotic trajectories, double and one well oscillation were observed as well as an additional trajectory existing between double well region. Trajectories were drawn by using an image processing code. Finally, ring/racetrack resonators were designed, manufactured and tested to be used in one or multiple NEMS detection. An experimental setup was developed for fast and easy alignment of fibers as well.

6.1 Focusing on Chaotic Trajectories

The experiments at Chapter 4 were mostly performed for comb drive voltage difference of 38 V meaning that height of the double well potential was mostly fixed. Similar experiments should be conducted for varying comb drive voltage differences to observe additional chaotic regions on the same nanomechanical buckling platform for varying potential well heights. Additionally, each trajectory should be investigated with discrete time steps (which could be half of the period) and statistical analysis of the trajectories should be made to differentiate the plastic deformation effect from the randomness of the trajectory.

6.2 Synchronized Chaos

Coupling two chaotic mechanical buckling beams at nano scale could open avenues to reveal rich nonlinear dynamics of such system and have potential to be used at complex computation and communication applications. For that, a preliminary design was developed. The most critical parameter here is to adjust the width of the mechanical beam coupling element which is essential for communication of the beams for synchronization. Width is calculated as 2 µm so it is fully suspended by using the same HF recipe that is used for manufacturing buckling devices. In summary, those devices are designed to be manufactured by using the same deposition and etching recipes for current devices.

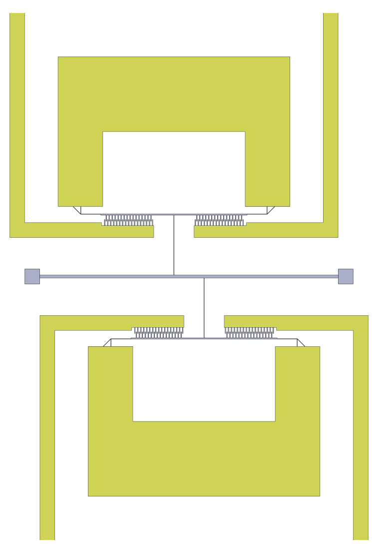

Figure 6.1: General look of design without the base silicon.

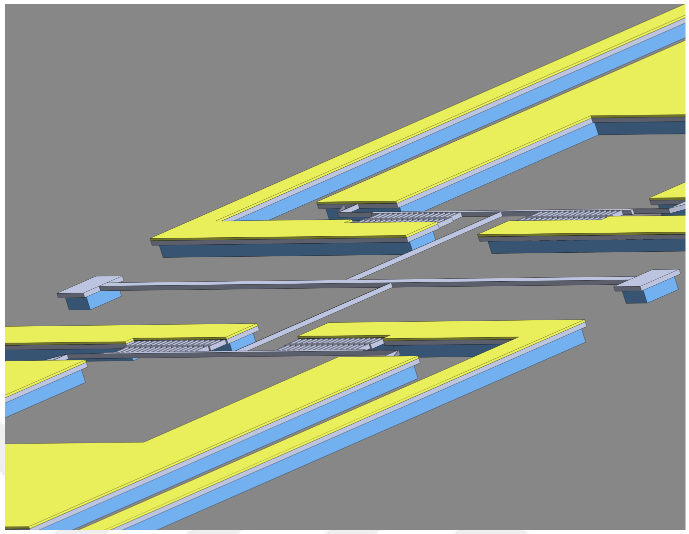

Figure 6.2: Tilted look of the device with base silicon.

6.3 Single and Multiple NEMS Measurements

By the ring/racetrack resonators developed, single or multiple NEMS and their interaction could be monitored. Additionally, since those systems provide large scale integration possibilities, by integrating those systems with array of fibers and electrospray ionization (ESI) techniques, sensor technologies for particle, virus and other bio/chemical detection could be developed either under vacuum or atmospheric pressures.

6.4 Measurement of Buckling Motion with Ring/Racetrack Resonators

Ring/racetrack resonators built can be integrated with nanomechanical buckling platforms for doing deflection measurement with error bars and noise floor levels even lower than the line mode method. Placing the beam so that the part largest displacement during buckling aligns with the center of the ring/racetrack resonator, will be enabling measurement of the mV level changes on the comb drive actuators.

Bibliography

[1] D. Rugar, R. Budakian, H. Mamin, and B. Chui, "Single spin detection by magnetic resonance force microscopy," *Nature*, vol. 430, no. 6997, pp. 329–332, 2004.

[2] T. P. Burg and S. R. Manalis, "Suspended microchannel resonators for biomolecular detection," *Applied Physics Letters*, vol. 83, no. 13, pp. 2698–2700, 2003.

[3] S. Schmid, M. Kurek, J. Q. Adolphsen, and A. Boisen, "Real-time single airborne nanoparticle detection with nanomechanical resonant filter-fiber," *Scientific reports*, vol. 3, no. 1, pp. 1–5, 2013.

[4] C.-H. Ke, N. Pugno, B. Peng, and H. Espinosa, "Experiments and modeling of carbon nanotube-based nems devices," *Journal of the Mechanics and Physics of Solids*, vol. 53, no. 6, pp. 1314–1333, 2005.

[5] W. Fon, M. H. Matheny, J. Li, L. Krayzman, M. C. Cross, R. M. D'Souza, J. P. Crutchfield, and M. L. Roukes, "Complex dynamical networks constructed with fully controllable nonlinear nanomechanical oscillators," *Nano letters*, vol. 17, no. 10, pp. 5977–5983, 2017.

[6] K. Ekinci, Y. Yang, X. Huang, and M. Roukes, "Balanced electronic detection of displacement in nanoelectromechanical systems," *Applied physics letters*, vol. 81, no. 12, pp. 2253–2255, 2002.

[7] S. S. Verbridge, H. G. Craighead, and J. M. Parpia, "A megahertz nanomechanical resonator with room temperature quality factor over a million," *Applied Physics Letters*, vol. 92, no. 1, p. 013112, 2008.

[8] I. Bargatin, E. Myers, J. Aldridge, C. Marcoux, P. Brianceau, L. Duraffourg, E. Colinet, S. Hentz, P. Andreucci, and M. Roukes, "Large-scale integration of nanoelectromechanical systems for gas sensing applications," *Nano letters*, vol. 12, no. 3, pp. 1269–1274, 2012.

[9] A. K. Naik, M. Hanay, W. Hiebert, X. Feng, and M. L. Roukes, "Towards single-molecule nanomechanical mass spectrometry," *Nature nanotechnology*, vol. 4, no. 7, pp. 445–450, 2009.

[10] M. S. Hanay, S. Kelber, A. Naik, D. Chi, S. Hentz, E. Bullard, E. Colinet, L. Duraffourg, and M. Roukes, "Single-protein nanomechanical mass spectrometry in real time," *Nature nanotechnology*, vol. 7, no. 9, pp. 602–608, 2012.

[11] M. S. Hanay, S. I. Kelber, C. D. O'Connell, P. Mulvaney, J. E. Sader, and M. L. Roukes, "Inertial imaging with nanomechanical systems," *Nature nanotechnology*, vol. 10, no. 4, pp. 339–344, 2015.

[12] J. E. Sader, M. S. Hanay, A. P. Neumann, and M. L. Roukes, "Mass spectrometry using nanomechanical systems: beyond the point-mass approximation," *Nano letters*, vol. 18, no. 3, pp. 1608–1614, 2018.

[13] K. Alzoubi, D. G. Saab, and M. Tabib-Azar, "Complementary nanoelectromechanical switches for ultra-low power embedded processors," in *Proceedings of the 19th ACM Great Lakes symposium on VLSI*, pp. 309–314, 2009.

[14] F. Chen, H. Kam, D. Markovic, T.-J. K. Liu, V. Stojanovic, and E. Alon, "Integrated circuit design with nem relays," in *2008 IEEE/ACM International Conference on Computer-Aided Design*, pp. 750–757, IEEE, 2008.

[15] M. Roukes, "Mechanical compution, redux?[nanoelectromechanical systems]," in *IEDM Technical Digest. IEEE International Electron Devices Meeting, 2004.*, pp. 539–542, IEEE, 2004.

[16] S. C. Masmanidis, R. B. Karabalin, I. De Vlaminck, G. Borghs, M. R. Freeman, and M. L. Roukes, "Multifunctional nanomechanical systems via tunably coupled piezoelectric actuation," *Science*, vol. 317, no. 5839, pp. 780–783, 2007.

[17] R. Yang, M. Xie, Y. Jia, L. Duraffourg, and P. X.-L. Feng, "Hybrid nanoelectromechanical switch and resistive memory in silicon nanowires by vlsi nems," in *2021 IEEE 34th International Conference on Micro Electro Mechanical Systems (MEMS)*, pp. 607–610, IEEE, 2021.

[18] T.-H. Lee, S. Bhunia, and M. Mehregany, "Electromechanical computing at 500 c with silicon carbide," *Science*, vol. 329, no. 5997, pp. 1316–1318, 2010.

[19] X. Wang, S. Narasimhan, A. Krishna, F. G. Wolff, S. Rajgopal, T.-H. Lee, M. Mehregany, and S. Bhunia, "High-temperature (¿ 500° c) reconfigurable computing using silicon carbide nems switches," in *2011 Design, Automation & Test in Europe*, pp. 1–6, IEEE, 2011.

[20] T. Chen, M. Pauly, and P. M. Reis, "A reprogrammable mechanical metamaterial with stable memory," *Nature*, vol. 589, no. 7842, pp. 386–390, 2021.

[21] B. Charlot, W. Sun, K. Yamashita, H. Fujita, and H. Toshiyoshi, "Bistable nanowire for micromechanical memory," *Journal of Micromechanics and Microengineering*, vol. 18, no. 4, p. 045005, 2008.

[22] L. Medina, R. Gilat, B. Robert Ilic, and S. Krylov, "Experimental dynamic trapping of electrostatically actuated bistable micro-beams," *Applied physics letters*, vol. 108, no. 7, p. 073503, 2016.

[23] M. Chiao and L. Lin, "Self-buckling of micromachined beams under resistive heating," *Journal of Microelectromechanical systems*, vol. 9, no. 1, pp. 146–151, 2000.

[24] D. Roodenburg, J. Spronck, H. Van der Zant, and W. Venstra, "Buckling beam micromechanical memory with on-chip readout," *Applied Physics Letters*, vol. 94, no. 18, p. 183501, 2009.

[25] S. O. Erbil, U. Hatipoglu, C. Yanik, M. Ghavami, A. B. Ari, M. Yuksel, and M. S. Hanay, "Full electrostatic control of nanomechanical buckling," *Physical review letters*, vol. 124, no. 4, p. 046101, 2020.

[26] B. R. Ilic, S. Krylov, M. Kondratovich, and H. G. Craighead, "Optically actuated nanoelectromechanical oscillators," *IEEE Journal of Selected Topics in Quantum Electronics*, vol. 13, no. 2, pp. 392–399, 2007.

[27] O. Basarir, S. Bramhavar, and K. Ekinci, "Motion transduction in nanoelectromechanical systems (nems) arrays using near-field optomechanical coupling," *Nano letters*, vol. 12, no. 2, pp. 534–539, 2012.

[28] D. Karabacak, T. Kouh, C. Huang, and K. Ekinci, "Optical knife-edge technique for nanomechanical displacement detection," *Applied physics letters*, vol. 88, no. 19, p. 193122, 2006.

[29] D. Y. Fedyanin and Y. V. Stebunov, "All-nanophotonic nems biosensor on a chip," *Scientific reports*, vol. 5, no. 1, pp. 1–12, 2015.

[30] K. Y. Fong, M. Poot, and H. X. Tang, "Nano-optomechanical resonators in microfluidics," *Nano letters*, vol. 15, no. 9, pp. 6116–6120, 2015.

[31] S. Stapfner, L. Ost, D. Hunger, J. Reichel, I. Favero, and E. M. Weig, "Cavity-enhanced optical detection of carbon nanotube brownian motion," *Applied Physics Letters*, vol. 102, no. 15, p. 151910, 2013.

[32] M. Maksymowych, J. Westwood-Bachman, A. Venkatasubramanian, and W. Hiebert, "Optomechanical spring enhanced mass sensing," *Applied Physics Letters*, vol. 115, no. 10, p. 101103, 2019.

[33] S. K. Roy, V. T. Sauer, J. N. Westwood-Bachman, A. Venkatasubramanian, and W. K. Hiebert, "Improving mechanical sensor performance through larger damping," *Science*, vol. 360, no. 6394, 2018.

[34] A. Venkatasubramanian, V. T. Sauer, S. K. Roy, M. Xia, D. S. Wishart, and W. K. Hiebert, "Nano-optomechanical systems for gas chromatography," *Nano letters*, vol. 16, no. 11, pp. 6975–6981, 2016.

[35] J. T. Gohring, P. S. Dale, and X. Fan, "Detection of her2 breast cancer biomarker using the opto-fluidic ring resonator biosensor," *Sensors and Actuators B: Chemical*, vol. 146, no. 1, pp. 226–230, 2010.

[36] A. Ksendzov and Y. Lin, "Integrated optics ring-resonator sensors for protein detection," *Optics letters*, vol. 30, no. 24, pp. 3344–3346, 2005.

[37] G. Anetsberger, O. Arcizet, Q. P. Unterreithmeier, R. Rivière, A. Schliesser, E. M. Weig, J. P. Kotthaus, and T. J. Kippenberg, "Near-field cavity optomechanics with nanomechanical oscillators," *Nature Physics*, vol. 5, no. 12, pp. 909–914, 2009.

[38] J. Chan, T. M. Alegre, A. H. Safavi-Naeini, J. T. Hill, A. Krause, S. Gröblacher, M. Aspelmeyer, and O. Painter, "Laser cooling of a nanomechanical oscillator into its quantum ground state," *Nature*, vol. 478, no. 7367, pp. 89–92, 2011.

[39] D. Vitali, S. Gigan, A. Ferreira, H. Böhm, P. Tombesi, A. Guerreiro, V. Vedral, A. Zeilinger, and M. Aspelmeyer, "Optomechanical entanglement between a movable mirror and a cavity field," *Physical review letters*, vol. 98, no. 3, p. 030405, 2007.

[40] A. Wallucks, I. Marinković, B. Hensen, R. Stockill, and S. Gröblacher, "A quantum memory at telecom wavelengths," *Nature Physics*, vol. 16, no. 7, pp. 772–777, 2020.

[41] L. Fan, C.-L. Zou, M. Poot, R. Cheng, X. Guo, X. Han, and H. X. Tang, "Integrated optomechanical single-photon frequency shifter," *Nature Photonics*, vol. 10, no. 12, pp. 766–770, 2016.

[42] M. Poot and H. X. Tang, "Broadband nanoelectromechanical phase shifting of light on a chip," *Applied Physics Letters*, vol. 104, no. 6, p. 061101, 2014.

[43] S. O. Erbil, *Design, fabrication, and applications of electrostatically buckled nanomechanical systems*. PhD thesis, Bilkent University, 2018.

[44] F. Moon and P. J. Holmes, "A magnetoelastic strange attractor," *Journal of Sound and Vibration*, vol. 65, no. 2, pp. 275–296, 1979.

[45] A. Yariv, “Critical coupling and its control in optical waveguide-ring resonator systems,” *IEEE Photonics Technology Letters*, vol. 14, no. 4, pp. 483–485, 2002.

Appendix A

MATLAB Codes

A.1 Line Mode Beam Detection

```
% Click once near the side gate.
    clear
    clc
    close all
    format long
    load line_mode_data.mat
    load scan_voltage.mat
    vol_divide = 5.3;
    num_voltage = 64;
    sampling_rate = 200e3;
```

```
seconds = 2.5;
number_of_points = 1:1:1e3;
repetition = 10;
beam_interval = 420;
beam_increment = 200;
gate_interval = 100;
gate_increment = 72;
scan_increment = 41770;
next_voltage_increment = 501191-30;
save_gate = zeros(1,repetition+1);
collect_mean = zeros(1,num_voltage);
collect_error_bar = zeros(1,num_voltage);
collect_single_position = zeros(num_voltage,repetition);
plot(denoised_signal);
hold on
plot(voltage_rs);
disp(['Click to record position.']);
roi1 = drawpoint;
p_click = roi1.Position;
```

```
current_dp_loc = round(p_click(1,1));
point_of_choice = current_dp_loc;
a = zeros(1,repetition);
[max_gate,index_gate] = max(denoised_signal(point_of_choice:1:
point_of_choice+gate_interval));
gate_position = point_of_choice+index_gate-1;
plot(gate_position,max_gate,'r*')
for i = 1:1:num_voltage
save_gate = zeros(1,repetition+1);
[max_gate,index_gate] = max(denoised_signal(gate_position:1:
gate_position+gate_interval));
gate_position = gate_position+index_gate-1;
plot(gate_position,max_gate,'r*')
for k = 1:1:repetition
save_gate(k) = gate_position;
[max_beam,index_beam] = max(denoised_signal(gate_position+
gate_increment:1:gate_position+
gate_increment+beam_interval));
beam_position = gate_position+gate_increment+index_beam-1;
```

```
plot(beam_position,max_beam,'r*')
a(1,k) = beam_position-gate_position;
[max_gate,index_gate] = max(denoised_signal(gate_position+
scan_increment-gate_interval/8:1:
gate_position+scan_increment+gate_interval/8));
gate_position = gate_position+scan_increment-gate_interval/8+
index_gate-1;
plot(gate_position,max_gate,'r*')
end
collect_single_position(i,:) = a;
collect_mean(i) = mean(a);
collect_error_bar(i) = std(a)/sqrt(length(a));
disp('Error bar is: ')
disp(std(a)/sqrt(length(a)))
disp('Mean is :')
disp(mean(a));
disp('Voltage is: ')
disp(i)
gate_position = save_gate(1)+next_voltage_increment;
```

end

A.2 Chaos Experiments Image Processing

% Adjust contrast at the beginning, 0.58 is the default value.

```
clear
clc
close all
start_pixel = 328;
end_pixel = 328;
repetition = end_pixel-start_pixel+1;
collect_trajectory = zeros(1,repetition);
collect_error_bar = zeros(1,repetition);
for l = start_pixel:1:end_pixel
I = im2double(imread(strcat('frame',num2str(l),'.tif')));
filtered_I = medfilt2(I(:,:,1),[3,3]); % salt n pepper filter
figure;
imshow(filtered_I);
title('SEM image with salt n pepper filter');
prompt = 'Is image good? (y/n): ';
```

```
str_sem = input(prompt,'s');
close
if str_sem == 'n'
trajectory_position = 0;
beam_pixel_number = 0;
else
black_n_white = imbinarize(filtered_I(:,:,1),0.58); %(making a binary image)
for px = 1:1:943
for py = 1:1:1024
if black_n_white(px,py,:) == 0;
black_n_white(px,py,:) = 1;
else
black_n_white(px,py,:) = 0;
end
end
end
figure;
imshow(black_n_white);
prompt = 'Is constrast good? (y/n): ';
```

```
str_contrast = input(prompt,'s');
while str_contrast == 'n'
prompt = 'Enter contrast between 0-1: ';
str_contrast_adjust = input(prompt,'s');
black_n_white = imbinarize(filtered_I(:,:,1),str2double(str_contrast_adjust));
for px = 1:1:943
for py = 1:1:1024
if black_n_white(px,py,:) == 0;
black_n_white(px,py,:) = 1;
else
black_n_white(px,py,:) = 0;
end
end
end
imshow(black_n_white);
prompt = 'Is constrast good? (y/n): ';
str_contrast = input(prompt,'s');
end
start_pixel_x = 550;
```

```
start_pixel_y = 576;

while black_n_white(start_pixel_x,start_pixel_y,:)==1;

start_pixel_x = start_pixel_x-1;

end

while black_n_white(start_pixel_x-3,start_pixel_y,:)==0;

start_pixel_y = start_pixel_y-1;

end

[x,y] = ginput(1);

x = ceil(x);

y = ceil(y);

scan_amount = 15;

collect_beam = zeros(1,scan_amount);

counter_beam = 0;

counter_error = 0;

beam_position = zeros(1,scan_amount);

counter_beam_pixel = 0;

for i = 1:1:scan_amount

collect_beam(i) = black_n_white(start_pixel_x-60,x-i,:);

black_n_white(start_pixel_x-60,x-i,:)=0;
```

```
if collect_beam(i) == 0
beam_position(i) = x-i;
counter_beam_pixel = counter_beam_pixel+1;
end
end
imshow(black_n_white)
pause;
beam_position_modified = zeros(1,counter_beam_pixel);
beam_position_counter = 1;
for i = 1:1:scan_amount
if collect_beam(i) == 0
beam_position_modified(beam_position_counter) = beam_position(i);
beam_position_counter = beam_position_counter+1;
end
end
beam_pixel_number = length(beam_position_modified);
trajectory_position = sum(beam_position_modified)/
length(beam_position_modified)-start_pixel_y
end
```

```
collect_trajectory(l-(start_pixel-1)) = trajectory_position;

collect_error_bar(l-(start_pixel-1)) = beam_pixel_number;

close;

disp(l);

end
```

Appendix B

LabVIEW Block Diagram for Optomechanics Experiments

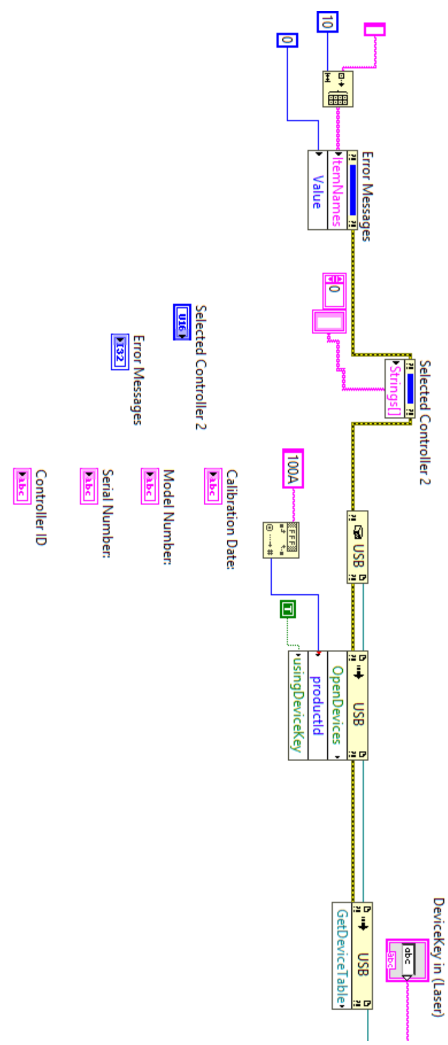
Error Messages
itemNames
Value
10
0
Selected Controller 2
Strings[]
100A
USB
OpenDevices
productId
usingDeviceKey
GetDeviceTable
DeviceKey in (Laser)
Selected Controller 2
Error Messages
Calibration Date:
Model Number:
Serial Number:
Controller ID

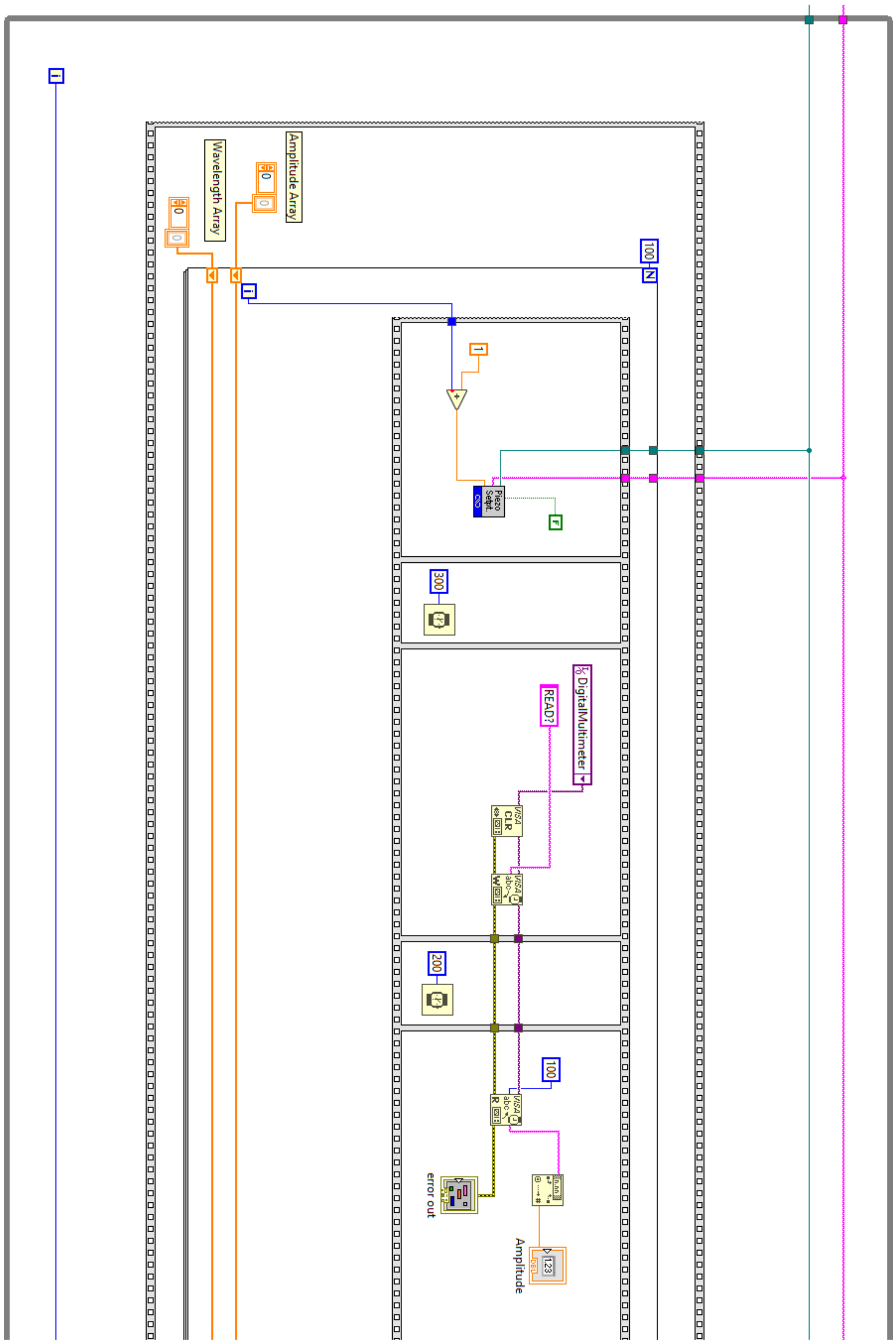
Wavelength Array
Amplitude Array
100
N
1
Piezo Setpt
F
300
DigitalMultimeter
READ?
VISA
CLR
W
200
100
R
error out
Amplitude

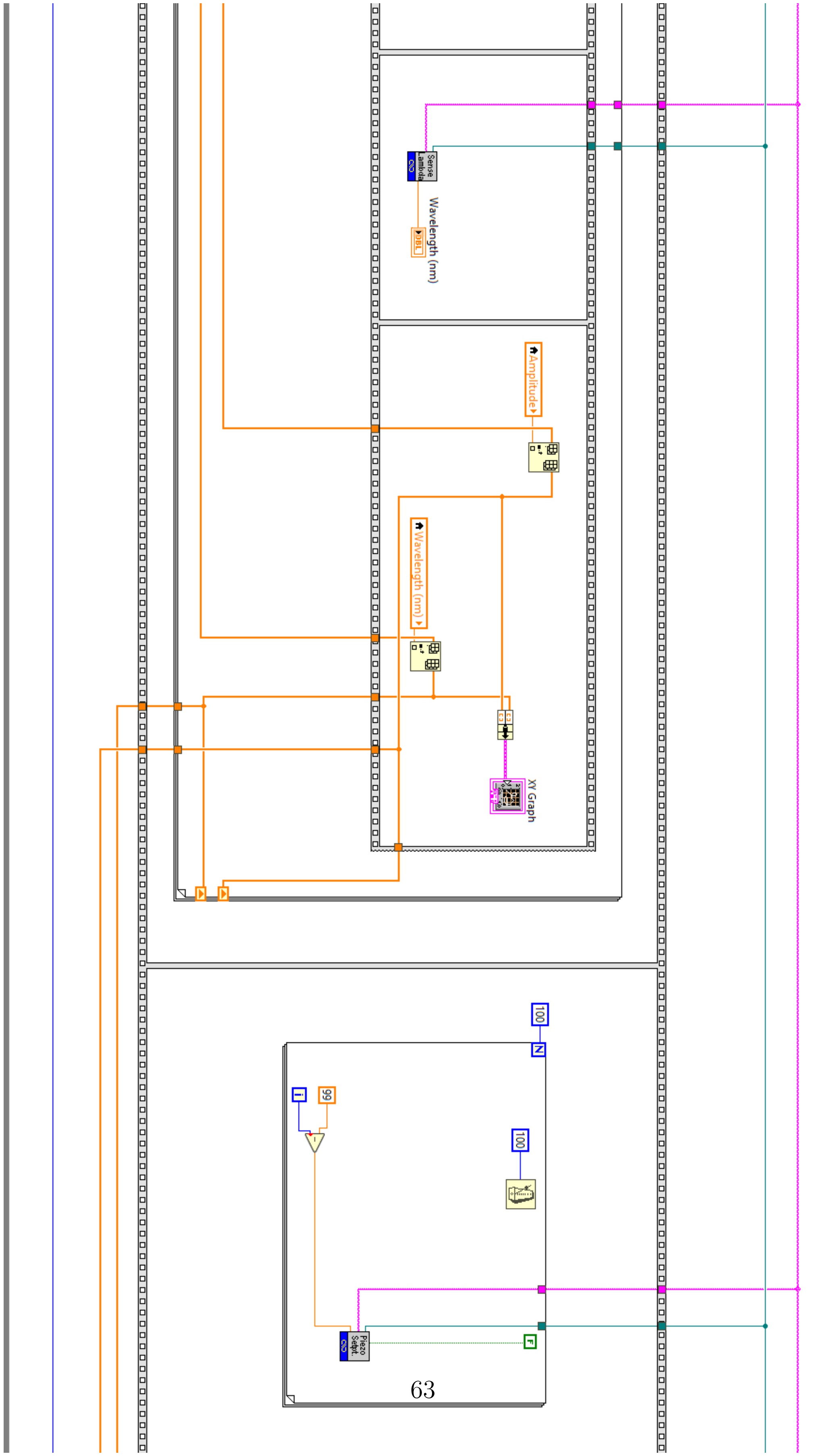
Sense Lambda
Wavelength (nm)
DBL
Amplitude
Wavelength (nm)
XY Graph
100
N
i
99
100
Piezo Setpt
F

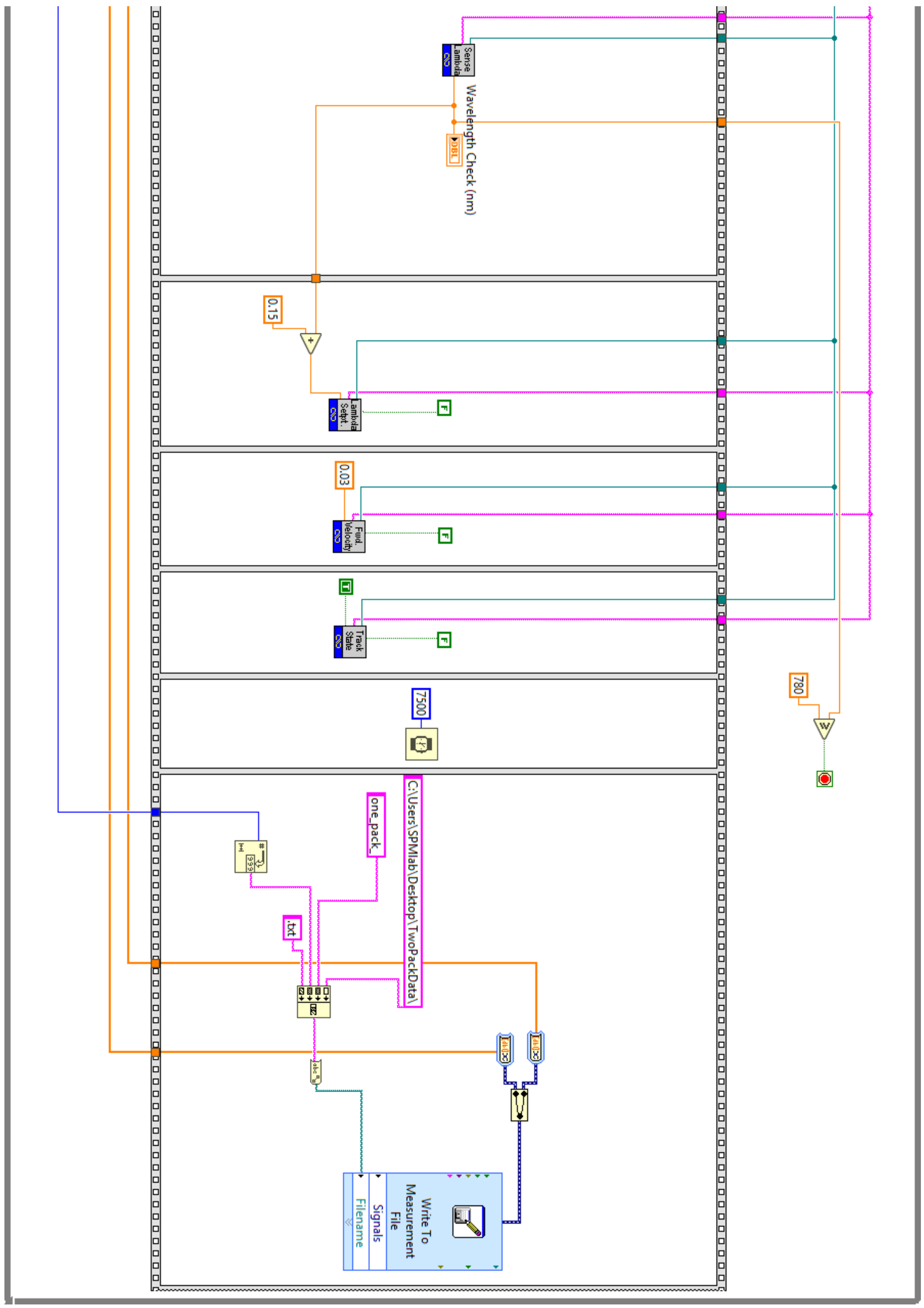
Sense Lambda
Wavelength Check (nm)
0.15
Lambda Setpt
0.03
Fwd. Velocity
Track State
7500
780
one_pack_
.txt
C:\Users\SPMlab\Desktop\TwoPackData\
Write To Measurement File
Signals
Filename